# Alkali pyroxenes and amphiboles: a window on rare earth elements and other high field strength elements behavior through the magmatic-hydrothermal transition of peralkaline granitic systems

Cyrielle Bernard, Guillaume Estrade, Stefano Salvi, Didier Béziat, Martin Smith

**HAL Id: hal-02989854**
**https://hal.archives-ouvertes.fr/hal-02989854**

Submitted on 5 Nov 2020

1 **Alkali pyroxenes and amphiboles: a window on Rare Earth Elements and other High Field Strength**

2 **Elements behavior through the magmatic-hydrothermal transition of peralkaline granitic systems**

3

4 Cyrielle Bernard[a], Guillaume Estrade[a□], Stefano Salvi[a], Didier Béziat[a] , Martin Smith[b]

5 [a] GET, CNRS, UPS, Université de Toulouse III, Toulouse, France

6 [b] School of Environment and Technology, University of Brighton, Brighton, BN2 4GJ, UK

7

8 □ Corresponding author: guillaume.estrade@get.omp.eu

9 ORCID: 0000-0001-6907-7469

10

11

19

20

21

22

23

24

**Abstract**

Peralkaline granites and pegmatites are a prime repository of REE and HFSE, critical raw materials. Although it is accepted that magmatic processes are fundamental in concentrating these metals, the role of hydrothermal fluids in concentrating and fractionating these elements remains unclear. This paper investigates the global reproducibility of the magmatic-hydrothermal evolution of alkaline silica-saturated systems using alkali pyroxene and amphiboles from six alkaline complexes. These minerals contain significant amounts of REE and other HFSE, and pyroxene is stable throughout the magmatic and hydrothermal stages. Amphibole consists of mostly unzoned arfvedsonite, leakeite, and katophorite, while pyroxene is always aegirine. Two types of aegirine were defined. In all complexes, type-I aegirine is zoned; its core is enriched in Ca, REE, Zr, Hf, Sc and Sn, and the rims in Na, $Fe^{3+}$ and contain secondary rare-metal bearing minerals and fluid inclusions. Type-II aegirine replaces amphibole and is oscillatory zoned. We interpret the amphiboles and REE-rich cores of type-I aegirine to have grown during the magmatic stage, whereas the rims of REE-poorer type-I and II aegirine formed during the hydrothermal stage. During magmatic crystallization, REE intake into amphiboles and pyroxene as well as LREE-HREE fractionation were favored by their crystallographic properties and by competition among them and other minerals. During subsequent hydrothermal stages, REE and other HFSE were remobilized, locally reconcentrated and fractionated in mineral pseudomorphs and secondary pyroxene. These observations point out the importance of studying rock-forming minerals such as pyroxenes and amphiboles to unravel geological events controlled by common processes globally.

**Keywords**

Peralkaline granite, pegmatite, pyroxene, amphibole, rare earth elements, high field strength elements

**Introduction**

High Field Strength Elements (HFSE, namely Nb, Ta, Zr, Hf, U, Th, Sn, and Ti), and in particular Rare Earth Elements (REE), are among raw materials considered the most critical today (European Commission 2018). They are used in many modern technologies linked to the transition to renewable energy infrastructure

53 (Lucas et al. 2014; Goodenough et al. 2018), but their production is quite restricted, worldwide. REE deposits

54 can be primary (igneous, carbonatites and alkaline systems) or secondary (placers and ion-adsorption)

55 (Chakhmouradian and Wall 2012) and economic concentrations of heavy REE (HREE, Gd to Lu) are rather rare

56 compared to those of light REE (LREE, La to Eu). The latter occur in high amounts mostly in carbonatites and

57 placer deposits and are commonly hosted in fluorcarbonates such as bastnäsite-(Ce), parisite-(Ce) and

58 synchysite-(Ce), and phosphate such as monazite-(Ce). Ion-adsorption deposits provide most of the global HREE

59 production (Chakhmouradian and Wall 2012; U. S. Geological Survey 2019). In alkaline igneous rocks, REE are

60 hosted mainly in monazite-(Ce), xenotime-(Y), fergusonite-(Y), loparite-(Ce) and eudialyte-group minerals

61 (EGM) (Larsen and Sørensen 1987; Chakhmouradian and Wall 2012). Most alkaline igneous rocks are silica-

62 undersaturated, with the silica-saturated variety (i.e., granitic) being quite rare (e.g. Larsen and Sørensen 1987;

63 Ranløv and Dymek 1991; Foland et al. 1993; Kramm and Kogarko 1994; Sheard et al. 2012). However, it is the

64 latter that have high Yb/La ratios compared to other varieties (Fig 1). Pegmatites, which form from the last and

65 most evolved part of silica saturated melts, concentrate the highest amounts of REE and other HFSE.

66      There is a general consensus in the literature that magmatic processes play a role for a pre-enrichment

67 of alkaline rocks in REE and other HFSE (Marks and Markl 2017). These include sourcing from undepleted,

68 more or less metasomatized mantle, crustal contamination, fractional crystallization, and melt-melt immiscibility

69 during magma cooling (Bonin 2007; Nardi and Bitencourt 2009; Chakhmouradian and Zaitsev 2012; Veksler et

70 al. 2012). There is also evidence that hydrothermal processes may play a key role in concentrating these

71 elements to ore grades (e.g. Salvi and Williams-Jones 1990; William-Jones et al. 2012). However, to date, the

72 relative importance of magmatic versus hydrothermal processes is still debated, partly because the processes

73 occurring at the magmatic-hydrothermal transition are hard to document and most studies were carried out in the

74 laboratory (e.g. Migdisov et al. 2016).

75      To fill this gap, it is important to understand the timing of concentration of the REE in natural occurrences.

76 To do so, in this paper we propose for the first time a detailed study of common minerals that carry REE and

77 other HFSE from the magmatic through the hydrothermal stages, from six silica-saturated alkaline occurrences

78 worldwide. The goal is to make out the meaning of textures and link them to the major events that impacted the

79 selected complexes, i.e. the magmatic-hydrothermal transition. Once it is clear which zones of the crystals grew

80 during the magmatic phase and which grew during hydrothermal circulations, we can analyze the REE and other

81 HFSE compositions in the different zones, and infer the timing of concentration and fractionation of the REE.

82 Ideal candidates to do so are the pyroxene and amphibole mineral groups, because of their ubiquitous presence in

83  these rocks and because they have been documented to form during a large span of the evolution of alkaline

84  rocks, from early magmatic to late hydrothermal stages (e.g. Nielsen 1979; Jones and Peckett 1981; Ranløv and

85  Dymek 1991; Marks et al. 2004). In addition, they incorporate a relatively high amount of REE and other HFSE

86  compared to other rock-forming minerals (e.g. alkali feldspar and quartz), even though they are not considered as

87  ore as their partition coefficients for HFSE (except Eu) are not high enough (Fedele et al. 2015). Primary

88  zirconosilicates can also incorporate high levels of HFSE and are common in alkaline rocks, however, they are

89  frequently altered to secondary minerals during the hydrothermal stage. Hence, pyroxenes and amphiboles are

90  the best minerals to evidence the behavior of HFSE throughout the entire process of alkaline granite and

91  pegmatite crystallization.

92

93  **1.  <u>Geological background</u>**

94  The six alkaline igneous complexes on which this work focuses are: Ambohimirahavavy (Estrade et al.

95  2014a) and Manongarivo (Donnot 1963) in Madagascar, Amis in Namibia (Schmitt et al. 2002), Evisa in Corsica

96  (Bonin et al. 1978), Khan Bogd in Mongolia (Kovalenko et al. 2006), and Strange Lake in Canada (Currie 1985).

97  These complexes were chosen because all present evidence of hydrothermal circulation and contain high

98  amounts of REE (from 800 ppm in a granite from Khan Bogd to 12 % in a pegmatite from Strange Lake,

99  unpublished data). All complexes contain peralkaline rocks, i.e. their ratio of $(Na_2O+K_2O)/Al_2O_3$ is >1. Some of

100  them have been the subject of in-depth studies, such as the Strange Lake complex which was first studied in the

101  late 1980's (e.g. Miller, 1986; Salvi and Williams-Jones 1990) and still is today (Vasyukova and Williams-Jones

102  2020); others are poorly known, as is the case for the Manongarivo complex, for which the only available

103  information is a mere mention in a French compilation (Donnot, <u>1</u>963).

104  Although they were emplaced in different geodynamic complexes and at different periods, it appears that the

105  melt source was a metasomatized upper mantle for all six complexes. Crustal contamination and feldspars

106  fractionation, if occurring, are two processes that can enrich alkaline granites in REE. However, the rate of

107  partial melting at the origin of these complexes is still debated, which is an essential parameter given that a lower

108  rate implies a greater accumulation of incompatible elements, REE included, in the newly generated melt. All

109  complexes underwent at least one alteration episode from an orthomagmatic fluid, and some of them an

110  additional late hydrothermal event (identified at Amis, Evisa, and Strange Lake). The composition of the fluids

111  that circulated was measured in fluid inclusions at Ambohimirahavavy and Strange Lake, and inferred from the

4

112  study of secondary mineral assemblages for the other complexes. The presence of significant amounts of $Na^+$

113  and $Fe^{3+}$ in an orthomagmatic fluid is reported for Evisa, the two Malagasy complexes and Strange Lake, and

114  $Ca^{2+}$ was identified at Khan Bogd, Madagascar and Strange Lake. Locally, $CO_2$ and/or $CH_4$ were reported at

115  Khan Bogd and Strange Lake, and $CO_3^{2-}$ at Amis. The resulting conclusions are similar for all the complexes:

116  independently of its orthomagmatic or late origin, a F-, Ca-rich fluid is systematically observed and inferred to

117  have mobilized and fractionated the REE. The importance of this process compared to magmatic ones in

118  concentrating and fractionating the REE is still a matter of debate. Comparing six complexes that were emplaced

119  in different geodynamic settings and witnessed different fluid conditions (composition, temperature), is a

120  strategy to highlight common features in order to better constrain and generalize the timing of REE and other

121  HFSE enrichment in alkaline complexes. Below, follows a rapid summary of the main geological features of

122  each complex; more detailed information is provided in Online Resource 1.

123

124  *1.1. Amis complex, Namibia*

125  The Amis complex and the larger Brandberg complex onto which it is juxtaposed are of the same age (132.5

126  to 130.5 My) and are hosted in metasediments of the Damara orogen (~ 550 My; Miller 1983) and volcanic

127  rocks from the Paraná-Etendeka igneous province. Three granite and 4 pegmatite-aplite samples were used for

128  this study. The Amis complex is mainly made of an arfvedsonite granite and aegirine-rich pegmatite-aplites. The

129  Amis complex is highly enriched in REE, other HFSE and volatiles ($H_2O$, F). Pegmatites and aplites in the

130  north-western part of the Amis complex are particularly enriched in REE mineralizations and uranium. Schmitt

131  et al. (2002) infer that hydrothermal fluids had a very limited impact on the rocks of Amis complex. They affirm

132  that minerals are all mainly magmatic, with the exception of replacement of arfvedsonite by quartz-hematite

133  overgrowths. Based on the study of melt inclusions, they propose that the main process of REE and other HFSE

134  enrichment is magmatic. In contrast, Diehl (1990) proposed that hydrothermal fluids played a significant role,

135  and inferred the replacement of arfvedsonite by aegirine.

136  *1.2. Evisa complex, Corsica*

137

138  The Evisa complex (290 My; Cocherie et al. 2005) was emplaced among metaluminous granitoids. We

139  collected 7 granite and 5 pegmatite samples from the central part of the complex. The complex mainly comprises

140  hypersolvus (perthitic feldspar) and subsolvus (albitic and alkali feldspar) peralkaline granites (Bonin 1990) and

5

141    associated pegmatites rich in REE-bearing minerals such as monazite-(Ce), apatite, and allanite-(Ce). The

142    hypersolvus granite probably experienced two hydrothermal events: a minor, early episode at the end of

143    crystallization, and a more important second episode, characterized by F-rich fluids, around 200 My (Poitrasson

144    et al. 1998; Bonin et al. 2008). The subsolvus granite is intrusive into the perthitic unit and only experienced the

145    second hydrothermal event, which triggered the replacement of the primary zirconosilicate elpidite by a

146    secondary assemblage (Bonin 1990).

147

148    *1.3. Khan Bogd complex, Mongolia*

149    The Khan Bogd complex is located in the southern Gobi Desert, at the transition between island-arc calc-alkaline

150    differentiated volcanics (329±5 My) and rift-related bimodal basalt–comendite–alkali granite association (318-

151    290 My), and is dated at approximately 290 Ma (Kovalenko et al. 2006). It is among the largest alkaline granite

152    plutons in the world, with a surface area of 1500 km². We collected 3 granite and 7 pegmatite samples, mostly on

153    the western side of the complex. The pluton consists of two ring bodies: a western peralkaline arfvedsonite-

154    bearing granite and a later emplaced, eastern aegirine granite. They are both associated with pegmatites. The

155    pluton has been investigated for mining purposes and estimates indicate grades between 0.3 and 4.5 % REE, the

156    highest grade being located at the top of the granite plutons (estimation of the tonnage is not available,

157    Kovalenko and Yarmolyuk 1995). The origin of this pluton is linked to a mantle plume and the continental

158    subduction of the South Mongolian Hercynides, but the exact magmatic process is still debated (Kovalenko et al.

159    2006; Kynicky et al. 2011). Kynicky et al. (2011) propose the release of a silica-saturated orthomagmatic fluid

160    that, similarly to Evisa, triggered the replacement of primary elpidite.

161

162    *1.4. Manongarivo and Ambohimirahavavy complexes, Madagascar*

163

164    Ambohimirahavavy and Manongarivo are the biggest complexes of the Ampasindava province in

165    northwestern Madagascar, yet are not well documented. They were emplaced at circa 24 Ma into marine-shelf

166    carbonates and marine-fluvial siliciclastic sediments of the Isalo Group (Thomas et al. 2009; Cucciniello et al.

167    2016). We collected 3 granite and 4 pegmatite samples from the southern part of the Ambohimirahavavy

168    complex. Due to poor outcropping conditions and low occurrence of pegmatites, we could only obtain 3

169  pegmatite samples from Manongarivo. The samples from Ambohimirahavavy were selected according to

170  previous studies from Estrade et al. (2014a, b). Both complexes were likely emplaced in a rifting context and are

171  made of two ring-shaped intrusions side by side, composed of nepheline syenite, alkali feldspar syenite, biotite

172  granite, peralkaline pegmatites, and various volcanic rocks. Due to the recent discovery of rare metals in

173  economic concentrations in ion-adsorption clays, the province drew the attention of a mining exploration

174  company (Estrade et al. 2014b). Granite and pegmatite dykes are the most enriched lithologies in REE and other

175  HFSE. An orthomagmatic fluid metasomatized the complexes in the very last stages of magmatic evolution

176  (Estrade et al. 2014b) and caused the replacement of primary zirconosilicates (eudialyte group minerals (EGM)

177  at Ambohimirahavavy, unknown at Manongarivo) by an assemblage of secondary HFSE-bearing minerals

178  (Lacroix 1923; Rakotovao et al. 2009; Estrade et al. 2018).

179

180  *1.5. Strange Lake complex, Canada*

181  The Strange Lake complex was emplaced 1240 My ago into Paleoproterozoic gneisses and quartz

182  monzonite (Miller 1996) and is considered to represent an extension of the Gardar rift in Greenland (Pillet et al.

183  1989; Boily and Williams-Jones 1994; Siegel et al. 2017a). We chose 3 granite and 4 pegmatite samples which

184  were selected according to previous studies from Salvi and Williams-Jones (1990, 2006; 1995). The Strange

185  Lake complex consists of a hypersolvus granite, while a younger, largely metasomatized transsolvus granite

186  (rare perthite plus two distinct feldspars, previously classified as subsolvus, e.g. Boily and Williams Jones, 1994)

187  surrounds it, forming the majority of the complex (Gysi et al. 2016; Siegel et al. 2017b). These plutons are

188  partially bounded by an outwardly-dipping fracture associated with fluorite and hematite breccia. Two zones of

189  pegmatites have been reported: the Main zone in the center of the complex, and the B zone on the northwestern

190  edge. These magmatic events correlate with a progressive enrichment in REE and other HFSE, from HFSE-poor

191  hypersolvus granite to HFSE-rich transsolvus granite and pegmatites (Miller 1996). Most of the REE are

192  concentrated in the pegmatites. Reserves are estimated at 278 Mt grading 0.93% $REE_2O_3$ of which 39% are

193  HREE, and 214 Mt at 0.85 % $REE_2O_3$ in total (Gowans et al. 2017). The complex also contains significant

194  amounts of $ZrO_2$, $Nb_2O_5$, and BeO. Two main extensive hydrothermal events affected the complex. The first

195  event is attributed to circulation of a hot ($\geq 300\,°C$) orthomagmatic brine consisting of K- and Na-enriched

196  aqueous and carbonic phases (Salvi and Williams-Jones 2006; Vasyukova and Williams-Jones 2019). The

7

197 second hydrothermal event consists of a cooler fluid (100 - 200 °C) resulting from mixing of a meteoric fluid

198 and a fluid originating from the granites (Gysi et al. 2016).

199

200

201 **2.** **Features common to pegmatites and granites from all six complexes**

202     Pegmatites in all complexes are heterogeneous in texture, i.e. they show mineralogical layering visible from

203 the scale of the outcrop to that of a thin section (Fig 3), whereas granites are generally homogeneous. In

204 pegmatites, the layers have grain sizes ranging from a few μm to about 40 cm and locally more (Fig 3).

205 Therefore, to obtain meaningful data, samples for this study were selected from zones of relatively fine grain size

206 (less than a few cm).

207     All pegmatites and granites are dominated by quartz, alkali feldspar (perthites, albite, orthoclase, and/or

208 microcline) that are commonly strongly albitized, plus alkali amphiboles and, mostly in pegmatites, aegirine

209 (Fig 4). Common minerals in both rock types include zircon, pyrochlore group minerals (PGM) and Fe- and Ti-

210 oxides. Other minerals present mostly in pegmatites include Ca and Na zirconosilicates, fluorite, astrophyllite

211 and REE-bearing minerals (typically bastnäsite-(Ce), monazite-(Ce), xenotime-(Y), chevkinite-(Ce), allanite-

212 (Ce), aeschynite-(Y), fergusonite-(Y), britholite-(Y), synchysite-(Ce)). Ti-bearing minerals such as chevkinite-

213 (Ce) and astrophyllite show signs of alteration such as dissolved edges (Fig 4a).

214     Ca and Na zirconosilicates, which are characteristic minerals of agpaitic rocks, are mostly eudialyte-group

215 minerals (EGM) at Ambohimirahavavy (Lacroix 1923; Estrade et al. 2018), and elpidite at Evisa, Khan Bogd

216 and Strange Lake (Bonin 1988; Salvi and Williams-Jones 1990; Grigor'eva et al. 2011). These zirconosilicates

217 were partially to totally replaced by secondary miaskitic mineral assemblages, which commonly form

218 pseudomorphs (Poitrasson et al. 1998; Estrade et al. 2014b; Gysi et al. 2016). The mineralogy of the

219 pseudomorphs varies in the different complexes and consists either of different Zr- and/or REE-bearing minerals

220 (Fig. 4b), or exclusively zircon plus quartz, i.e. typical miaskitic mineral assemblage (Fig 4c). Both

221 pseudomorph types are found in all complexes, except in Amis where our samples only contain the miaskitic

222 zircon-quartz type. Elpidite can also be extensively replaced by other zirconosilicates, namely armstrongite and

223 gittinsite (e.g. Salvi and William-Jones 1995), whereas EGM is only partially replaced by these phases. At Khan

224 Bogd, cathodoluminescence reveals the elpidite is altered from its core, replaced by zircon and armstrongite (Fig

225 4d). Pseudomorphs from Evisa consist of Ca-rich mineral assemblages such as fluorite and parisite-(Ce), the

226  latter growing mostly at the expense of bastnäsite-(Ce). At Manongarivo and Amis, the precursor mineral has not

227  been identified because partial replacement has not been observed in these complexes, so far.

228

229      3.  **Analytical methods**

230      Polished thin sections were prepared from all samples from the six complexes and were studied using

231  transmitted light microscopy, cathodoluminescence, Scanning Electron Microscopy (SEM), microprobe, and

232  Laser-Ablation Inductively Coupled Plasma Mass Spectrometry (LA-ICPMS) in order to determine mineral

233  textural relationships and amphiboles and pyroxene zoning.

234      SEM images in back-scattered electron (BSE) mode were collected with a Jeol JSM6360LV SEM coupled

235  with a Bruker silicon drift detector and interpreted with the Esprit software at the Géosciences Environnement

236  Toulouse laboratory, using an accelerating voltage of 20 kV, and a detection time of 40 s.

237      Mineral compositions were determined at the Centre Raymond Castaing in Toulouse, using a CAMECA

238  SX Five electron microprobe (EPMA), with an accelerating voltage of 15 kV, a beam current of 20 nA for

239  pyroxene, 10 nA for amphibole, and a beam diameter of about 2 μm. Quantitative elemental maps were

240  performed on the same instrument, using an accelerating voltage of 15 kV, a beam current of 20 nA and 100 nA

241  for major and minor elements respectively. Counting time was 1 s on each pixel with a step of 0.5 to 4 μm

242  depending on crystal size. Uncertainties were calculated using the method of Ancey et al. (1978). Standards used

243  for calibration as well as detection limits based on repeated measurements are provided in Online Ressource 2.

244      To resolve the oxidation state of iron measured by microprobe, calculations of the valence were made

245  following Droop (1987). In order to verify these measurements, a $^{57}$Fe Mössbauer spectrum was collected at the

246  Laboratoire de Chimie de Coordination - University of Toulouse on a constant-acceleration conventional

247  spectrometer, at 80 K and with a 1.85 GBq source of 57Co, over a ±12 mm/s range with 512 channels. The

248  spectra were acquired via a compact detector c-system and recorded with a Canberra multichannel analyzer,

249  coupled to a computer with Recoil Mossbauer Analysis Software 1.05 from Lagarec and Rancourt (1997).

250  Uncertainties were calculated using the covariance matrix. Pyroxene end-members were then calculated

251  following Mann et al. (2006). Amphiboles end-members were calculated using the spreadsheet available from

252  Locock (2014).

253       Trace element concentrations were determined in situ by LA-ICPMS at the Géosciences Environnement

254    Toulouse laboratory, University of Toulouse, on 30-µm polished thin-sections, using a New Wave Research ESI

255    213 laser coupled to a Thermo-Fisher Element-XR high-resolution ICP-MS. Laser beam diameter varied from 30

256    to 50 µm depending on mineral size, and data were acquired by ablating lines instead of spots in order to prevent

257    intersecting solid inclusion or internal zoning. NIST synthetic glass certified reference materials SRM 610 and

258    SRM 612 were used as external and quality control standards, respectively. Each analysis was normalized using

259    $SiO_2$ values previously determined by EMPA. The relative precision ranged from 5 to 10% and detection limits,

260    based on repeated measurements, are provided in Online Ressource 3. Trace elements maps were performed at

261    the Trinity College in Dublin according to the method provided in Ubide et al. (2015) using photon machines

262    G2 193 nm UV laser with a Helex two-volume cell coupled to a Thermo iCAPQ ICP-MS. Laser beam spot for

263    maps was 12 µm square, scan speed 8 µm/s and repetition rate 41 Hz. NIST SRM 610 glass was used as

264    standard. A beam size of 12 µm square typically allows a spatial resolution of 7-10 µm in x and y. This relatively

265    new ablation technique removes only 3-4 µm of material, which allows several maps to be performed on the

266    same area. A first map with all REE and other HFSE was first established, before acquiring a second map with

267    only 5 elements in order to obtain a better signal. LA-ICP-MS maps provide detailed spatial information on

268    zonation in crystals that would not be available otherwise. Analysis were semi-quantitative and compared to

269    microprobe data to obtain the real concentration.

270       To check for the absence of REE mineral inclusions in the pyroxene, we analyzed one sample from the

271    Amis complex by Scanning Transmission Electron Microscopy (STEM) at the Centre Raymond Castaing in

272    Toulouse. Unlike TEM, with STEM the electron beam is focused on a specific point of the sample and scans its

273    surface instead of being focused on the entire surface. This allows a better resolution as well as local chemical

274    identification (e.g. Pennycook and Nellist 2011). The Focused Ion Beam (FIB) was used to prepare the sample

275    for STEM. The FIB is a Hélios 600i operated at 5 kV, and the TEM a JEOL cold-FEG JEM-ARM200F operated

276    at 200 kV equipped with a Cs probe corrector reaching a spatial resolution of 0.078 nm. Images were acquired in

277    high-angle dark field (HAADF) as well as bright field (BF) modes. EDX spectra were recorded on a

278    JEOL CENTURIO SDD detector.

279

280    **4.    Amphibole and pyroxene textural and chemical description**

281    *4.1. Textural features*

*4.1.1. Amphiboles*

283    Amphiboles occur in granites and pegmatites as well-developed euhedral crystals (Fig 4e). No significant

284    textural difference was found between amphiboles of the six complexes. They all appear pleochroic, dark green

285    or dark blue to black under plain polarized light (PPL). Their size is highly variable from one complex to another

286    as well as inside pegmatites (typically ranging from 20 μm to 10 cm), but is always comparable with the size of

287    quartz and alkali feldspar crystals in the same rock. Except at Evisa (Fig 4j), amphiboles are not zoned, but they

288    display dissolution/corrosion textures on their rims. They commonly have small quartz and feldspar inclusions,

289    and are in equilibrium with these minerals. Replacement of amphiboles by aegirine and Ti- and/or Fe-oxides is a

290    common feature of peralkaline granitoids (Marks and Markl 2017) and occurs in all pegmatites and some

291    granites (Fig 4e).

292

293    *4.1.2. Pyroxene*

294    Pyroxene is ubiquitous in pegmatites and granites of all six complexes but present three different

295    textural features. (1) In pegmatites which contain only minor amphibole, it occurs as light to dark green euhedral

296    crystals under PPL ranging from 50 μm to 10 cm. These pyroxene crystals present a core-to-rim zonation

297    pattern, with additional sector zoning in the rims, which are visible under PPL (Fig 4f). Similarly to amphiboles,

298    these crystals are in equilibrium with quartz and alkali feldspar grains. In the rims of this pyroxene, we also

299    found fluid inclusions (Fig 4g) and mineral inclusions that match the composition of those met in pseudomorphs

300    (Fig 4b and h). These pyroxene crystals were found in all studied complexes but Strange Lake. At Khan Bogd,

301    these crystals present an additional zoning area between the core and the sector zoned rims (Fig 4k). (2) In some

302    pegmatites, pyroxene occurs as anhedral crystals of size similar to the one we just described. These crystals are

303    oscillatory zoned, from yellowish to green under PPL (Fig 4i). They commonly include Fe- and/or Ti- oxides.

304    (3) In granites as well as in some pegmatites, anhedral pyroxene is found replacing amphibole (Fig 4e). This

305    pyroxene is also weakly oscillatory zoned. As it replaces amphibole only partially, it's size is smaller than the

306    previously described pyroxene crystals and depends on the original amphibole size. This pyroxene is associated

307    with Fe- and/or Ti- oxides and can sometimes keep the 120° cleavages from the original amphibole.

308    Based on occurrence, size, color, zoning and mineralogical associations, we distinguish two main types of

309    pyroxene in the six complexes we focus on in this study. Type-I matches euhedral zoned pyroxene, and our

310    study focuses mainly on this type. Based on the observation that they present anhedral shape, oscillatory zoning,

311 and are associated with Fe- and/or Ti- oxides, we regroup anhedral single pyroxene crystals and pyroxene

312 replacing amphibole under the denomination type-II.

313

### 4.2. Major element composition

#### 4.2.1. Amphiboles

316    Since they present the same textural features, all amphiboles were identified based solely on their

317 chemistry, following the classification of Hawthorne et al. (2012) and in accordance with Leake et al. (1997).

318 The general formula of amphibole is $AB_2C_5T_8O_{22}W_2$ where, in this study, A = Na; B = Na, Ca; C = $Fe^{2+}$, $Fe^{3+}$,

319 Li; T = Ca, Al; and W = OH, F. The rootname is given to these amphiboles based on the composition of the sites

320 A, B and C, and the prefix is added according to the composition of the sites C and W. By strictly following

321 these rules, it appears that some complexes contain only one amphibole type, common to granites and

322 pegmatites, and some contain different amphiboles (Table 1). Ambohimirahavavy (ferro-ferri-fluoro-leakeite;

323 $Na_3Fe_4LiSi_8O_{22}F_2$), Manongarivo and Strange Lake (fluoro-arfvedsonite; $Na_3Fe_5Si_8O_{22}F_2$), and Khan Bogd

324 (arfvedsonite; $Na_3Fe_5Si_8O_{22}(F,OH)_2$) contain only one amphibole. At Amis, amphibole is ferro-ferri-fluoro-

325 leakeite in pegmatites and fluoro-arfvedsonite in the granite. At Evisa, granites and pegmatites contain a zoned

326 amphibole with a core of fluoro-arfvedsonite and a rim of ferro-ferri-fluoro-leakeite (Fig 4L). In addition, the

327 hypersolvus granite from Evisa contains zoned crystals with ferro-ferri-katophorite

328 $(Na_2Ca(Fe^{2+},Mg)_4Fe^{3+}(Si_7Al)O_{22}(OH)_2)$ in their core and fluoro-arfvedsonite in their rims (Fig 4j).

329    However, it is important to keep in mind that amphibole is a solid solution, thereby two amphiboles can

330 have different names but be close in composition, and inversely can have the same name but present a

331 compositional range. To avoid these artificial hiatuses and subsets, we focused on the concentration of elements

332 involved, when attributing amphibole names in this study. Hence, the distinction between katophorite and other

333 amphiboles is based on the Ca/(Ca+Na) ratio; being >0.25 (close to 0.4), this makes it a Na-Ca amphibole,

334 compared to values <0.1 for other amphiboles, which are then considered Na-amphiboles. Thereby, ferro-ferri-

335 katophorite at Evisa exhibits a significant compositional gap with the other amphiboles from this study. The

336 distinction between Na-amphiboles is more subtle, and is based on the amount of Li and $Fe^{2+}/Fe^{3+}$ ratio in the C

337 site. Ideally, leakeite has 1 Li apfu; this value is on average 0.6 apfu at Ambohimirahavavy and Evisa, and 0.7

338 apfu at Amis. Arfvedsonites from the other complexes have average Li contents of 0.1-0.3 apfu, validating the

339 distinction proposed here, although these values are intermediate between the two categories. The prefixes ferro-

340 and ferri- refer to the presence of $Fe^{2+}$ and $Fe^{3+}$, respectively, in the C site.The prefix fluoro- indicates that the F

341 concentration is systematically higher than the concentration of other elements in the W site. In this study, the

342 amounts of F and OH, respectively, are close to 1.1 and 0.9 apfu in arfvedsonite from all complexes but Khan

343 Bogd, where it is closer to 0.9 apfu F and 1.1 apfu OH. Strictly complying with the definition would result in two

344 different names (F and OH varieties), which would vary with each complex. However, this would lead to add

345 unnecessary confusion to the nomenclature, therefore, because the compositional differences are only minor, we

346 chose to ignore this parameter.

347        Within a given category, amphiboles are globally similar in composition in all complexes, including

348 $Fe^{2+}/Fe^{3+}$ (around 3 for fluoro-arfvedsonite, 2 for leakeite, and 3.5 for katophorite), with only local variations

349 (Table 1). Chlorine was not detected by microprobe analyses in any of the amphiboles. The main distinction

350 regarding major element composition is found in (fluoro)-arfvedsonite from Manongarivo and Khan Bogd,

351 which both have high contents of Mn (respectively 1.92 and 1.66 % vs 0.50 % in the other complexes, Fig 5d)

352 and $Fe^{2+}/Fe^{3+}$ (4.00 and 5.90 vs 2.40). Amphibole from Ambohimirahavavy is also rich in Mn (1.99 %) but does

353 not show a high $Fe^{2+}/Fe^{3+}$ value. Fluoro-arfvedsonite from Amis is as rich in F as ferro-ferri-fluoro-leakeite from

354 all other complexes (around 1.6 apfu), which is unusual (Deer et al. 1997b). Amphiboles from pegmatites are

355 generally slightly richer in HFSE, Li and $Fe^{3+}$ than amphiboles from granites.

356

357        *4.2.2. Pyroxene*

358        Based on composition, pyroxene in granites and pegmatites consists of 85 to 97 % aegirine end-

359 member. Therefore, according to the classification of Morimoto (1988), we will refer to it as aegirine in the

360 following sections of this paper. Pyroxene from Ambohimirahavavy and Khan Bogd is more Ca-rich than the

361 other complexes, but it is still classified as aegirine.

362        Type-I aegirine crystals show a characteristic zoning pattern in pegmatites from all locations: a core-to-

363 rim zoning visible in BSE images (Fig 6n) and a sector zoning visible even by optical microscopy (Fig 6o). This

364 pattern defines 3 main zones, where zone A is the core and zones C and D form sector-zoned rims. Zone C

365 matches the crystallographic sector (110), and zone D sector (100) (Ubide et al. 2019). In a few cases, an

366 additional zone matching the crystallographic sector (010) is also present (e.g. ESM 6). All zones are optically

367 distinguished by different tones of green, attributed to different Ti contents (Fig 6g) (e.g. Strong 1969; Ferguson

368 1973; Nielsen 1979). The contacts between different zoning are sharp in all occurrences (Fig 6). Zone A, the

core, is systematically enriched in Ca, Sn, Hf, Zr (Fig 7a, b, c, g) and depleted in Na, Al and $Fe^{3+}$ compared to the other zones (Table 3). In pegmatites, we measured up to 2 wt% $ZrO_2$ in aegirine cores; although uncommon, Zr-rich aegirine was also described in other localities such as in nepheline syenites from the Motzfeldt Centre, South Greenland (Jones and Peckett 1981; up to 7 wt% $ZrO_2$) and in metaluminous trachytes from the Warrumbungle Volcano, Australia (Duggan 1988; up to 14.5 wt% $ZrO_2$). Sector zone C is particularly enriched in Ti and Ca (Fig 6e, g), while D is in Fe (Fig 6c). Two major growth layers are visible in the rims with, in sector C, Ti and Ca decreasing towards the rims of each layer (Fig 6e, g). Al content is low in aegirine from all six complexes (about 0.3 % $Al_2O_3$ compared to standard average values of 1.2 % reported in aegirine; e.g. Deer et al. 1997a). At Khan Bogd, an additional zone, referred to as zone B, is found between the core and the sector-zoned rims of the crystals (Fig 4k); it shows random oscillations due to variations in many elements, including Ti and Mn. The same zoning pattern, including zone B, was also observed by Ranløv and Dymek (1991) in nepheline syenite from the Narssaq Peninsula. However, they only documented variations in Zr, Ti, Al, Na, Ca and Fe. Larsen (1976) and Piilonen et al. (1998) respectively described a core-to-rim zoning in aegirine from nepheline syenite in the Ilímaussaq and Mont Saint-Hilaire complexes. They report cores enriched in Ca, $Fe^{2+}$, Mg, Mn and Zr compared to rims, which in turn contain higher Al, Ti, Na and $Fe^{3+}$. Shearer and Larsen (1994) supplemented the description of aegirine from Ilímaussaq, by reporting Sr and REE enrichment in cores compared to rims. In our analyses, we did not observe a systematic difference in Mn and Sr contents between core and rims.

Type-II aegirine is not sector-zoned but shows oscillatory zoning and we observed a wide variety of compositions depending on which layer was analyzed (Table 2). This zoning is irregular, with no core, made of compositionally varying layers with variable thickness. No common pattern was found among any type-II aegirine crystals, beside their heterogeneity. Many elements are involved, including Fe, Mn, Ca, and Ti (see Online Resource 8). No significant chemical differences were found between type-II aegirine from granites and pegmatites. Type-II aegirine is commonly depleted in Ti and Sn compared to type-I aegirine, except at Khan Bogd. Mg is commonly found in higher concentration in type-II aegirine (Table 2). No significant compositional difference was found between type-II aegirine replacing amphibole in granite and those in pegmatites. At Strange Lake, all observed aegirine crystals are of type-II (Table 2; Salvi and Williams-Jones 1990; Roelofsen 1997).

14

*4.3. Trace element composition*

*4.3.1. Amphiboles*

400      Amphiboles from all six complexes have very similar trace element patterns (Table 1). Fluoro-
401 arfvedsonite and ferri-fluoro-leakeite have practically the same composition, with Li contents alone being
402 responsible for the transition from one kind to the other. This cation enters the amphibole structure according to
403 the substitution: $^{C}Li^{+} + {}^{C}Fe^{3+} = 2^{C}Fe^{2+}$, described by Hawthorne et al. (1996). Ferro-ferri-katophorite, which is
404 more calcic than the two other amphiboles, relates to fluoro-arfvedsonite through the substitution: $^{B}Ca^{2+} + {}^{T}Al^{3+}$
405 $= {}^{B}Na^{+} + {}^{T}Si^{4+}$ (Deer et al. 1997b). This last substitution increases the size of the C site, leaving more space to
406 incorporate LREE. Similarly, the coupled substitution (Mg, $Fe^{2+}$) $\rightarrow$ $Fe^{3+}$ occurring in the C site of amphiboles
407 enhances HREE incorporation (Bottazzi et al. 1999; Siegel et al. 2017b). Amphibole chondrite-normalized REE
408 patterns are systematically enriched in HREE relative to LREE, with a depression in medium REE (MREE, from
409 Eu to Dy). This pattern is unusual compared to more Ca-rich amphibole compositions in which REE patterns are
410 usually enriched in LREE or in MREE (e.g. Marks et al. 2004; Coint et al. 2013). All spectra display a negative
411 Eu anomaly suggesting early plagioclase fractionation (Fig 8). The absolute REE concentrations, though
412 somewhat varying from one complex to another, are quite similar (Fig 8).

413      Despite their similar patterns, the absolute concentrations of REE and other HFSE can vary in
414 amphiboles from one complex to the other. Fluoro-arfvedsonite from Manongarivo and Khan Bogd both have
415 low quantities of Sn (4 and 10 ppm) and HREE (35 and 50 ppm on average). Fluoro-arfvedsonite from
416 Manongarivo also has less LREE than fluoro-arfvedsonite from other complexes (11 vs 60 ppm on average).
417 Ferro-ferri-katophorite from Evisa displays high enrichments in LREE and HREE (respectively 224 and 290
418 ppm) (Fig 8). Ferro-ferri-fluoro-leakeite from Amis is notably different from other complexes in terms of trace
419 elements: it is richer than ferro-ferri-fluoro-leakeite from other complexes in Ti (0.18 vs 0.07 apfu), Sn (360 vs
420 32 ppm), Zn (0.24 vs 0.05 apfu), Pb (97 vs 7 ppm), LREE (168 vs 37 ppm on average) and HREE (140 vs 83
421 ppm on average) (Table 1, Fig 5d). Mn and Zn vary together on a 1:1 relation at Strange Lake, as mentioned in
422 the paper by Hawthorne et al. (2001). Mn and Zn covary in amphiboles from Ambohimirahavavy and Amis as
423 well, but in a different way (respectively 4:1 and 1:3), while at Manongarivo and Khan Bogd they do not appear
424 to be related.

425

*4.3.2. Pyroxene*

427    Type-I aegirine, similarly to amphiboles, presents comparable trace elements patterns but different

428    absolute concentrations, from one complex to the other (Table 2). Cores of type-I aegirine from the two

429    Malagasy complexes have high Zr concentrations compared to other complexes (> 8000 vs 2700 ppm on average

430    for the other complexes). Khan Bogd aegirine is poorer in Li (17 vs 115 ppm), LREE (12 vs 80 ppm on average)

431    and HREE (21 vs 125 ppm on average). Type-I aegirine from Amis, similarly to ferro-ferri-fluoro-leakeite in this

432    complex, shows quite a different trace chemistry than aegirine from other complexes. Average Li is low (50 vs

433    115 ppm), while other metals are high, e.g. Zn (1780 vs 435 ppm), Sn (3740 vs 700 ppm), Pb (39 vs 7 ppm) and

434    U (29 vs 0.5 ppm) (Table 2 and Fig 7g). REE and Sc contents in cores of type-I aegirine (zone A) are higher than

435    in the rims (zones B, C and D) for all complexes (Fig 6, 9 and Table 3; similar maps of aegirine crystals from

436    each complex are provided in Online Resource 4 to 8). Inside the rims, sector zone C is systematically enriched

437    in REE compared to sector D (Fig 6k, l, m). Nb and Ta do not have a constant behavior: their contents can be

438    higher in sector zone C, be present only in fractures, or be enriched in an independent zonation, with all three

439    cases being possible within the same sample. Similarly to amphiboles, the chondrite-normalized REE patterns of

440    aegirine show high values for HREE relative to LREE, with lower medium REE. This particular pattern is

441    known to be specific to Na- and Fe-enriched aegirine (Mahood and Stimac 1990; Shearer and Larsen 1994). The

442    absolute REE concentrations, are quite similar from one complex to another, although small variations do exist

443    (Fig 9).

444    Trace element concentrations in type-II aegirine are highly dependent on the zoning pattern. This is

445    notably true for Sn, Hf and Zr. Compared to type-I aegirine, Sn covaries with Ti instead of Zr. The shape of

446    type-II aegirine REE patterns is similar to that of type-I, i.e. high HREE relative to LREE, with a depression in

447    medium REE and a negative Eu anomaly. There is no common pattern in the REE contents of type-II aegirine:

448    REE contents are higher in type-II than in type-I aegirine at Khan Bogd, generally lower at Evisa, and have

449    similar values in Madagascar and at Amis (Fig 7g).

450    To verify that the concentrations of REE measured in aegirine truly result from their incorporation in

451    the crystal structure and not from small mineral inclusions, we used a STEM approach to investigate the core of

452    a type-I aegirine, where REE are most concentrated. We did not detect any REE mineral inclusion, validating the

453    premise that the REE are indeed incorporated in the pyroxene's structure. The main substitution involved in this

454    process is common to type-I aegirine from all pegmatites. The classic aegirine substitution is

455    $^{M2}Ca^{2+} + {}^{M1}(Mg^{2+}, Fe^{2+}) \leftrightarrow {}^{M2}Na^{+} + {}^{M1}Fe^{3+}$.                (Eq. 1)

456    However, in aegirine from this study there is not enough $Fe^{3+}$ to equilibrate this reaction, hence Al, Zr and Ti,

457    present in aegirine, also contribute to compensate this deficiency, resulting in a new substitution mechanism:

458    $^{M2}Ca^{2+} + {}^{M1}(Mg^{2+}, Fe^{2+}) \leftrightarrow {}^{M2}Na^{+} + {}^{M1}(Fe^{3+}, Al^{3+}, Zr^{4+}, Ti^{4+})$.         (Eq. 2)
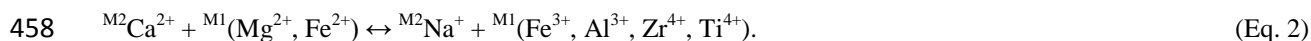
459    However, REE can enter both M1 and M2 sites along with $Fe^{3+}$ and $Na^{+}$ (Beard et al. 2019). In clinopyroxenes,

460    incorporation of REE, as well as other HFSE, is controlled by five crystal-chemistry driven mechanisms, with

461    site parameters being determined by the size of the major elements. The first mechanism is decreasing

462    temperature and increasing melt alkalinity, which usually lowers the REE compatibility. The second mechanism

463    is similar to that for amphiboles and is defined by the substitution Ca → Na, which increases the size of the M2

464    site leaving more space to incorporate LREE. It also decreases the size of the M1 site, making it more adequate

465    to incorporate HREE. The third mechanism takes place in the M1 crystallographic site, where the combined

466    substitution $(Mg, Fe^{2+}) \rightarrow Fe^{3+}$ leads to a charge effects that allows more HREE to enter this site along with $Fe^{3+}$

467    (Marks et al. 2004; Beard et al. 2019). The fourth mechanism, described by Mollo et al. (2017), is also due to a

468    charge effect. These authors propose the coupled substitution

469    $^{M1}(Al, Fe^{3+}) + {}^{T}Al \leftrightarrow {}^{M2}(Mg, Fe^{2+}) + {}^{T}Si$,         (Eq. 3)

470    whereby the increase in Al at the expense of Si creates a charge deficiency compensated by the incorporation of

471    REE in the M2 site. In addition, the growth from an environment rich in REE can result in incorporation of high

472    levels of REE in aegirine. Indeed, the adsorption of REE onto aegirine surface during supersaturation may be too

473    fast to equilibrate as crystal growth rate exceeds the internal diffusion rate (Smith et al. 2004).

474    All of the above mechanisms have the potential of favoring the incorporation of REE into pyroxene,

475    however, aegirine in our study having low $^{T}Al$ and practically no Mg or $Fe^{2+}$ in the M2 site, the mechanism of

476    Mollo et al. is probably not significant in this case. The high REE concentration in aegirine of this study is

477    therefore probably the result of the four other mechanisms that rely on size, charge, and kinetics effect at M sites

478    of aegirine.

479

480    *4.3.3. Ce anomalies*

481    Some amphibole and aegirine chondrite-normalized spectra, mostly from one pegmatite sample from

482    Amis, display a peak in Ce concentration (Fig 8 and 9). The occurrence of this peak being restricted to a few

483    samples, mass interference is excluded. In addition, ICP-MS signals showing peaks during ablation were all

484 excluded so the presence of this Ce peak is not due to mineral inclusions. This peak may be due to the presence

485 of $Ce^{4+}$ instead of the usual $Ce^{3+}$. Indeed, $Ce^{4+}$ has a smaller ionic radius (0.97 Å) than $Ce^{3+}$ (1.143 Å) for an

486 eight-fold coordination, thereby $Ce^{4+}$ substitutes more easily with $Fe^{2+}$ (0.92 Å) and $Mg^{2+}$ (0.89 Å; Shannon

487 1976). The change in oxidation state is commonly interpreted to indicate an increase in oxygen fugacity in the

488 environment that can be either low temperature magmatic (<600 °C, Trail et al. 2012) or hydrothermal (Xu et al.

489 2017).

490

### 5. Discussion

#### 5.1. *Origin of amphiboles*

493 In the previous sections we have seen that three different amphiboles can be distinguished based on

494 their major and trace chemistry: fluoro-arfvedsonite $(Na_3Fe_5Si_8O_{22}(F,OH)_2)$, ferri-fluoro-leakeite

495 $(Na_3Fe_4LiSi_8O_{22}F_2)$, and ferro-ferri-katophorite $(Na_2Ca(Fe^{2+},Mg)_4Fe^{3+}(Si_7Al)O_{22}(OH)_2)$. All of them occur in

496 granites and pegmatites as euhedral crystals and contain inclusions of quartz and feldspar grains (Fig 4e),

497 suggesting co-crystallization. Only amphiboles from Evisa have a variable composition, from fluoro-

498 arfvedsonite or ferro-ferri-katophorite in cores, respectively to ferri-fluoro-leakeite or fluoro-arfvedsonite in the

499 rims. In the other complexes, only one amphibole type is present in granites and in pegmatites. Based on textural

500 observations, we believe these changes are the sign of magmatic evolution. Indeed, the concentration of Li and

501 Na rises in the melt as differentiation occurs, until Li- and Na-rich amphiboles crystallize instead of their Li-

502 poor, Mg-, Ca-rich equivalents. Based on various pieces of evidence, such as having a similar age to that of

503 granite emplacement (Kovalenko et al. 2006), presence of melt inclusions (Schmitt et al. 2002), occurrence as

504 well-developed euhedral crystals, and dissolution/corrosion textures (Estrade et al. 2014a; Gysi et al. 2016), it is

505 accepted in the literature that amphiboles are magmatic phases in peralkaline granites. Hence, in accordance with

506 our observations and those in the literature about the six studied complexes, we conclude that amphiboles of all

507 types in our samples are magmatic. Their variation in trace element composition is directly linked to the

508 environment they grew in, a highly evolved melt, enriched in incompatible elements. Among incompatible

509 elements are the REE, which are known to be preferentially incorporated in alkaline amphiboles along with Na

510 for LREE and $Fe^{3+}$ for HREE (Bottazzi et al. 1999; Siegel et al. 2017b). Due to this crystallo-chemical control,

511 amphiboles can incorporate a lot of REE at the magmatic stage, with a preference for HREE. Slight

512 compositional differences in REE, Zn, Sn, Nb, Zr and Pb between amphiboles of the 6 complexes (Fig 5d) likely

513 reflect parental melt compositions. For example, the presence of ferro-ferri-katophorite in Evisa probably

514 indicates an effect of melt contamination in Ca by the surrounding aluminous granites.

515     As previously described, amphiboles are commonly altered to Fe- and Ti-oxides and to type-II aegirine.

516 Based on textural evidence that at Strange Lake this replacement occurs preferentially along cleavages in altered

517 granites and pegmatites, as well as on mass-balance calculations, Salvi and Williams Jones (1990) identified this

518 pyroxene occurrence as hydrothermal. Because we observed this replacement in all of our samples, it follows

519 that a late hydrothermal event is a common feature in the complexes studied and, by extrapolation, most likely in

520 alkaline rocks in general; indeed, a hydrothermal event was also documented in silica-undersaturated alkaline

521 rocks such as at Ilímaussaq (e.g. Borst et al. 2016) or at Khibina and Lovozero (e.g.Arzamastsev et al. 2011).

522 Gysi et al. (2016) and Vasyukova and Williams-Jones (2019) show that at Strange Lake this event is due to a

523 relatively high temperature, Ca-rich fluid. Based on the similarity of amphiboles alteration in all six complexes,

524 we infer that the circulation of an orthomagmatic fluid is a process common to all complexes.

525

526     *5.2.  Origin of pyroxene*

527         *5.2.1.    Core-to-rim zonation*

528     Even though both types of aegirine identified in all complexes show some kind of zonation, only type-I

529 shows a core-to-rim zonation, with a core enriched in Ca, Zr, Sn, Hf, Sc, REE and depleted in Na, Al and Fe

530 compared to the rims (Fig 6). The rims also have a higher $Fe^{3+}/ Fe^{2+}$ ratio than the core. This pattern is

531 systematic for type-I aegirine crystals from all complexes. Type-II aegirine is oscillatory zoned and can replace

532 amphibole.

533     The sharp compositional change between the core and the rims in type-I aegirine (Fig 6) suggests a

534 sudden change in the crystallizing environment. Based on the scarce presence of type-I aegirine where

535 amphiboles are present, we infer that they grew in competition. Only the rims C and D contain fine oscillatory

536 zoning (e.g. $TiO_2$ on Fig 6g), fluid inclusions (Fig 4g), and, at Ambohimirahavavy, mineral inclusions that match

537 the composition of those measured in hydrothermal pseudomorphs (e.g. zircon, bastnäsite-(Ce), Fig 4b and h).

538 Therefore, we infer that type-I aegirine has a magmatic core (zone A on Fig 6p) while the rims are hydrothermal

539 (zones C and D in Fig 6p). Zone B being only present at Khan Bogd, it will be discussed lower in this section.

540 Chemical zoning in aegirine of our rocks matches that observed by Piilonen et al. (1998) in aegirine from Mont

541 Saint-Hilaire, which they describe as a magmatic pyroxene overgrown by hydrothermal fibrous aegirine. More

542 details about each element in the different zones is provided in the following paragraphs.

543      The variations in Na, Ca, Al, and Fe can be explained by a common process. Type-I aegirine magmatic

544 cores are enriched in Ca, and its hydrothermal rims are richer in Na, Al and $Fe^{3+}$. Evidence such as widespread

545 feldspar albitization, fluid inclusions composition, and the hydrothermal growth of aegirine without amphibole

546 indicate that circulating hydrothermal fluids are oxidizing (above the magnetite-hematite buffer), of relatively

547 high pH and rich in NaCl among other phases (Salvi and Williams-Jones 1996; Smith 2007; Estrade 2014; Gysi

548 et al. 2016). Depletion in Ca and enrichment in Na and Fe while moving on from aegirine magmatic core to

549 hydrothermal rims can then be explained by intake of Na from the hydrothermal fluids and simultaneous

550 crystallization of Ca-rich secondary minerals in the pseudomorphs (fluorite, bastnäsite-(Ce)). This process

551 increases the amount of aegirine endmember compared to hedenbergite endmember which, along with the

552 hydrothermal environment being more oxidizing than the silicate melt, increases the $Fe^{3+}/ Fe^{2+}$ ratio in the rims.

553 The absolute amount of Al is very low in aegirine of this study, so the observed increase in this element in

554 aegirine rims can be linked only to charge effects, with $Al^{3+}$ being incorporated along with $Fe^{3+}$.

555      Because of their similar behavior, Zr and Hf both occur in the same growth zones. Based on the many

556 arguments in favor of a magmatic core and hydrothermal rims, we propose two hypotheses as to the

557 crystallization timing of type-I aegirine. Jones and Peckett (1981) asserted that formation of Zr-enriched aegirine

558 is enhanced by low oxygen fugacity, and can only occur if no other Zr-bearing phase is growing.  Pseudomorphs

559 after primary zirconosilicates were found around aegirine crystals (Fig 4b), hence it is impossible that aegirine

560 grew after the magmatic zirconosilicates. Our first hypothesis is that, in accordance with the observations made

561 by Jones and Peckett (1981), type-I aegirine cores grew before magmatic zirconosilicates, in the magma

562 chamber. In the absence of any mineral Zr has a strong affinity for, Zr partitioned mostly into aegirine. These

563 primary phenocrysts were brought into pegmatites, where primary zirconosilicates began to crystallize,

564 incorporating most of the available Zr.. Moving on to the hydrothermal stage, primary zirconosilicates were

565 destabilized and replaced by minerals richer in Zr, including zircon, which form the pseudomorphs. Aegirine

566 rims were then in competition with zircon, which has a high Zr uptake and therefore accounts for the decrease in

567 Zr concentration in aegirine rims. In this hypothesis, aegirine necessarily stopped growing during their migration

568 from the magma chamber to the pegmatites, or it would have resulted in another zonation in the magmatic core.

569 Our second hypothesis is that aegirine core and primary zirconosilicates grew at the same time. In this case the

570 conclusions of Jones and Peckett (1981) do not apply. This may be because their study was based on rocks from

571  the magmatic chamber of Ilímaussaq which had plenty of time to equilibrate during crystallization, whereas our

572  study is based on pegmatites, which crystallize quickly. Anyhow, in this hypothesis the competition between the

573  two minerals resulted in the preference of Zr to go into primary zirconosilicates, but because of the high content

574  of Zr in the melt and its low mobility (Duggan 1988), affinity for aegirine was still high enough to enrich it up to

575  the 2 wt% that we have measured. The subsequent hydrothermal stage is similar to the one in our previous

576  hypothesis, with higher Zr uptake by zircon rather than by zirconosilicates accounting for the decrease in Zr

577  concentration in aegirine rims. A similar behavior was observed for Sn and is most likely due to a similar

578  phenomenon. No Sn-based mineral was found in pseudomorphs, but $Sn^{4+}$ can easily enter in the composition of

579  secondary Ti-oxides because its radius is similar to the $Ti^{4+}$ ion in eight-fold coordination (Shannon 1976). In

580  addition, Sn is known to have a high solubility in Cl-rich fluids (e.g. Keppler and Wyllie 1991), making it easily

581  mobilized. This results in a much higher Sn content in the magmatic zone A than in the rims of aegirine. At

582  Amis, amphibole in pegmatite as well as aegirine are both enriched in Sn, Zn and Pb in comparison with the

583  other complexes of this study (Fig 7g). Ambohimirahavavy and Manongarivo have similar trace elements

584  concentration (Fig 7g) and formed in the same geological context, a few km away from each other. Both

585  amphibole and pyroxene from Khan Bogd have low trace elements concentrations. All these observations tend to

586  indicate that the variations of absolute concentration in REE, Zn, Sn, Zr, U and Pb between aegirine crystals of

587  the 6 complexes (Fig 7g), similarly to amphiboles, likely reflect parent melt compositions.

588

589  5.2.2.  *Sector zoning*

590  Sector zoning occurs in the most outer rims in type-I aegirine, involves variations in Ti, Ca, Fe and

591  REE, and was observed in all complexes. Many explanations have been invoked as to the origin of sector zoning,

592  and the latest agree on the fact that it is linked to a crystal growth faster than element diffusion rates (Ubide et al.

593  2019). If this condition is respected, it will result a disequilibrium between the different crystal faces that will not

594  all incorporate the same elements as it normally would (Strong 1969; Ferguson 1973; Larsen 1981). Elements

595  are however incorporated on the different crystal faces in a matter so that charge balance is respected (Ubide et

596  al. 2019). The crystallization rate could also impact the size of protosites (partially formed site on the surface of

597  a growing crystal), which are in equilibrium with the crystallizing environment, and preferentially incorporate

598  elements depending on their charge/radius ratio. If the growth rate is higher than ionic diffusion in the crystal,

599  the protosites will not have enough time to re-equilibrate in size and incorporate different elements on the

different faces of the crystal (Nakamura 1973). This higher growth rate is likely related to a lower temperature due to the change from magmatic to hydrothermal environment (Barkov and Martin 2015). However, these considerations must be taken carefully, as most of the research is based on augite and not aegirine.

Incorporation of Ti in aegirine is uncommon (Rønsbo et al. 1977; Dyulgerov and Platevoet 2006). Many explanations have been evoked: high temperature, low $fO_2$, high $fO_2$, low pressure, high activities of $TiO_2$ and $SiO_2$, high activity of alkalis, or a peculiar chemical composition of the environment such as low Zr and Na and high Ca (Ferguson 1973; Flower 1974; Larsen 1976; Rønsbo et al. 1977; Nielsen 1979; Brousse and Rançon 1984; Dyulgerov and Platevoet 2006). In our samples, a high temperature is ruled out as Ti incorporation occurs during the hydrothermal stage. As described in the previous section, Zr and Ca concentration are low in the crystallizing environment, and Na is high. Hence, and in accordance with Dyulgerov and Platevoet (2006), Larsen (1976), and Flower (1974), we suggest that in our rocks the incorporation of Ti into hydrothermal aegirine is favored by a high activity of Na and the low availability of Zr. Titanium may have been provided by the alteration of magmatic Ti-bearing minerals, such as astrophyllite (found at Manongarivo, Strange Lake, Khan Bogd and Amis, Fig 4a) chevkinite-(Ce) (found at Ambohimirahavavy, Manongarivo and Evisa), or others such as narsarsukite, låvenite, and aenigmatite.

### 5.2.3. Oscillatory zoning

Oscillatory zoning is present in both types of aegirine. In type-I, it is found in the sector zoned rims C (crystallographic sector (110)) and D (crystallographic sector (100)) as well as in zone B, intermediate between the core and the rims. Considering that zone B in type-I aegirine is only present in our samples in Khan Bogd, and was locally described in aegirine from the South Gardar Province, South Greenland by Ranløv and Dymek (1991), a general process to explain its formation is difficult to establish. Like zones C and D, zone B is poorer in Ca, Zr, Hf, Sn and REE than zone A. It is not specifically enriched in any element, but shows oscillatory zoning in Ti and Mn. We believe that zone B development is related to a specificity in the history of the Khan Bogd complex (Kynicky et al. 2011). In this complex, magmatic zone A aegirine would crystallize before or in competition with primary elpidite. At the hydrothermal stage, primary elpidite altered mostly into a secondary hydrated Ca- and REE-rich elpidite (Fig 4i), and zone B grew simultaneously. The uptake of Ca and Zr by secondary elpidite from the fluid led to the lower concentration of these elements observed in zone B. The final

stage, similarly to other complexes, was a more or less extensive pseudomorphism of elpidite and the formation

of zones C and D on aegirine.

Oscillating concentrations in zones C and D are most likely produced by autocatalytic surface

attachment, or boundary layer effect (Ortoleva et al. 1987; London 2008), which occurs when the crystal growth

rate exceeds the diffusion rate of components in the fluid. Consider an initial solution saturated in component A,

whose adsorption on the crystal surface is fast. As the adsorption progresses, the interface between the crystal

and the solution becomes depleted in component A, and switches to saturation in component B. Component B is

then adsorbed at the surface of the crystal, until the interface crystal-solution becomes saturated in component A

again. This process results in a rhythmic but irregular zoning of aegirine crystals in zones C and D, consistent

with a growth in a rapidly changing environment, which is a hydrothermal fluid.

Type-II aegirine either replaces amphibole or forms isolated crystals. Both kinds are found associated

with Fe- and/or Ti- oxides, and are randomly zoned in many elements (Ti, Ca, Mn, Fe, Hf, Sn, Zr at least). The

formation of aegirine from amphibole is known to be hydrothermal (e.g. Salvi and Williams-Jones 1990; Gysi et

al. 2016). For arfvedsonite, it follows the reaction provided by Salvi and Williams-Jones (1997):

$$3Na_3Fe_5Si_8O_{22}(F,OH)_2 + 2H_2O = 9NaFeSi_2O_6 + 2Fe_3O_4 + 6SiO_2 + 5H_2. \tag{Eq. 4}$$

The released Fe generally forms hematite or magnetite. Considering that zoning patterns are the same

for all type-II aegirine crystals and that they are systematically found associated with Fe- and/or Ti- oxides, we

consider that they all grew replacing amphibole, totally or partially. Hence, we consider type-II aegirine as

hydrothermal.


*5.3. REE behavior in amphiboles and aegirine*

As mentioned in the introduction, amphiboles and pyroxenes, in agreement with their crystal-chemical

parameters, can incorporate up to several hundreds of ppm of REE. In addition, their alkaline nature enhances

the fractionation of light versus heavy REE through the preferential incorporation of HREE in their structure,

resulting in the globally HREE-enriched patterns observed (Fig. 9; Beard et al. 2019). From the amphibole

compositions, we know that the melt was rich in F (Table 1). Beard et al. (2020) showed that the more F in the

melt, the lower the pyroxene-melt partition coefficient, hence the less REE are incorporated in pyroxene; this

affects the LREE more than the HREE and hence contributes to the observed globally HREE-enriched patterns.

656   The REE compositional patterns observed in type-I aegirine are similar to the compositional trends for

657   Zr, Hf and Sn, i.e. they are globally enriched in the core compared to the rims, except for Khan Bogd where the

658   opposite is true (Fig 10, Table 3). Given that the REE concentrations in aegirine at Khan Bogd are very low (2-7

659   ppm for Ce, 4-15 ppm for Y), we believe that this reverse trend is actually not significant (Fig 10). The

660   difference in REE concentration between aegirine zone A and zones B, C and D is due to the competition

661   between aegirine and zirconosilicates for these elements, during the magmatic stage for zone A, and during the

662   hydrothermal stage for the zones B, C and D. Scandium is sometimes grouped with REE, hence, it is not

663   surprising to observe that, similarly to REE, it is enriched in the core of type-I aegirine.

664   During the hydrothermal stage, aegirine is in competition with an altered, REE-enriched elpidite for

665   zone B, and with REE-bearing minerals in pseudomorphs (e.g. bastnäsite-(Ce)) for zones C - (110) and D -

666   (100). We therefore suggest that it is a competition for REE between aegirine and coprecipitating minerals

667   having each a different REE affinity which explains the variations in REE concentrations among the aegirine

668   core-to-rim zones. REE are also affected by sector zoning and are more concentrated in zone C than D, along

669   with Ti and Ca. Beard et al. (2019) studied experimentally the fractionation of REE in clinopyroxene in

670   peralkaline melts and showed that the more Na and less Ca in M2 site of pyroxene, the smaller the M1 site, and

671   the more HREE are incorporated. In addition, the authors mention that physico-chemical parameters not

672   recorded in the composition of clinopyroxene, such as pressure, also play a significant role in the size of the M1

673   site. However, this mechanism is well defined only for pyroxenes whose aegirine component is not higher than

674   50 %. In our samples, the substitution $Ca \rightarrow Na$ simply cannot be responsible for the zonation observed, as more

675   REE are found in the C sector, where Ca concentration is also higher. In addition, in Ca-rich pyroxenes such as

676   diopside and augite, Ca was not reported to fractionate between sectors (e.g. Ubide et al. 2019), which is another

677   argument for the occurrence of a different exchange mechanism in our samples.

678   In addition to the above variations in bulk abundance, cores and rims also preferentially incorporate

679   REE with lower or higher atomic numbers, creating a fractionation between the heavy and light REE. To

680   evaluate this process, we calculated the percentages of REE enrichment or depletion from core to rim in type-I

681   pyroxene. To do so, data obtained by LA-ICPMS were assigned either to the core or to the rim, based on their Zr

682   content and zoning SEM observations. By comparing these two parameters, we were able to determine a

683   threshold value, unique to each complex, below which a given aegirine analysis should be considered as rim, and

684   above which core. These data were averaged out to obtain a single value each for core and rim (Fig 10). Finally,

685   we calculated the extent of loss or enrichment between core and rim for each REE, according to:

686 $\quad d = \frac{C-R}{C} \times 100$ (Eq. 5)

687 where *d* represents the percentage difference between core and rim, *C* and *R* the mean values obtained for core

688 and rim, respectively. Error bars shown in Fig 11 were obtained using common error calculation formulae,

689 namely (Eq. 6) for the mean and (Eq. 7) for the percentage.

690 $\quad \overline{err} = \sqrt{\frac{\sum_{x=1}^{n}(err_x)^2}{n}}$ (Eq. 6)

691 $\quad d_{err} = \frac{C-R}{C} \sqrt{\frac{err_C^2 - err_R^2}{(C-R)^2} + \frac{err_C^2}{C^2}}$ (Eq. 7)

692 with $\overline{err}$ being the mean error, *n* the number of measurements, $d_{err}$ the error on the percentage variation from

693 core to rim, $err_C$ the mean error on core data, and $err_R$ the mean error on rim data. Resulting values indicate an

694 enrichment in that element in the rim compared to the core when positive, while negative ones indicate a

695 depletion (Fig 11).

696 $\qquad$ From the calculation of the percentage of depletion of REE from core to rim (Fig 11) we see that Amis,

697 Manongarivo and Evisa have a trend with a more important depletion of LREE than HREE: from 40-80 % to 20-

698 40 % depletion, respectively. Ambohimirahavavy shows the opposite trend: around 30 % of LREE depletion for

699 45% of HREE depletion. The latter trend is not as obvious as for other complexes, but it is still significant.

700

701 $\qquad$ *5.4. General model*

702 $\qquad$ We propose a global model of formation for amphiboles and aegirine in pegmatites (Fig 12). During the

703 magmatic stage, two hypotheses remain. In the first one, amphibole and zone A of type-I aegirine grew at early

704 magmatic stage, concentrating Zr and REE. In the second hypothesis, type-I aegirine core, amphibole and

705 zirconosilicates grew in competition. Most Zr was incorporated in the zirconosilicates, as well as REE if the

706 primary zirconosilicates was EGM. However, highly differentiated alkaline melts being particularly enriched in

707 Zr and REE, there is an extra supply in these metals which, combined with a fast crystallization, could be

708 incorporated by the structures of amphiboles and aegirine (Fig 12a).

709 $\qquad$ During the orthomagmatic hydrothermal stage, amphiboles did not grow anymore, and type-I aegirine

710 was in competition with secondary Zr- and REE-bearing minerals (generally zircon and bastnäsite-(Ce)) that

711 formed pseudomorphs after primary zirconosilicates. Since HFSE have much higher affinity for these secondary

712      minerals, their concentrations globally decreased in the co-crystallizing aegirine rims. It is also during this stage

713      that type-II aegirine crystals nucleated. Nevertheless, competition does not explain the observed LREE-HREE

714      fractionation. Residual melt, depleted in incompatible elements, likely crystallized late quartz and feldspar.

715      Given the overwhelming evidence for circulation of an orthomagmatic fluid in all complexes, we propose

716      that fractionation results from variations in fluid composition. From the presence of secondary minerals such as

717      bastnäsite-(Ce) and fluorite, and the study of fluid inclusions at Ambohimirahavavy and Strange Lake (Estrade

718      2014; Vasyukova et al. 2016), we know that the fluids contained at least the anions $Cl^-$, $F^-$, and $CO_3^{2-}$. These

719      species have the ability to form stable complexes with the REE, to different extents. $F^-$ and $CO_3^{2-}$ together are

720      mostly depositional ligands (Migdisov et al. 2016), thus precipitate with REE typically forming the LREE-

721      bearing bastnäsite-(Ce). On the other hand, $Cl^-$ is a weak but abundant ligand that can transport LREE more

722      easily than the heavy ones (Migdisov et al. 2016). If present as a transporting ligand, $F^-$ also transports more

723      LREE than HREE (Beard et al. 2020). We can thus infer that, depending on the relative concentrations of each

724      ligand, fractionation of light vs heavy REE would be specific to each complex (Fig 12b). As long as fluid flow

725      continued, aegirine rims kept growing, although REE incorporation and LREE-HREE fractionation kept

726      diminishing. By the time the hydrothermal stage waned, the two aegirine types were in equilibrium with the

727      pseudomorphs and the partially replaced amphiboles (Fig 12c).

728

729      6.   **Conclusions**

730

731      By comparing amphibole and pyroxene in six alkaline complexes worldwide, our study highlights that

732      despite different geodynamic contexts, mineralogy, and REE enrichment, there is a general crystallization

733      process common to all studied alkaline pegmatites. We believe this process can be generalized to all alkaline

734      $SiO_2$-saturated pegmatites worldwide, with local variations in mineralogy and REE-enrichment and fractionation

735      rates. This crystallization process includes at least two main stages, respectively magmatic and hydrothermal.

736      From the study of the composition of amphibole and type-I aegirine core, we document the magmatic stage,

737      during which a systematic primary enrichment in REE, HFSE and a LREE-HREE fractionation occurs. This

738      enrichment is common to all complexes and linked to the properties of the extremely differentiated alkaline

739      magma. The enrichment rate, however, differs from one complex to another. The REE fractionation is most

740 likely due to crystallographic properties of aegirine and alkali amphiboles that preferentially incorporate HREE

741 and do not represent an inherent property of the melt.

742 From the study of the texture and composition of type-I aegirine rims and type-II aegirine, we document

743 similarities between complexes during the hydrothermal stage, at which amphiboles stop growing, type-I

744 aegirine grows sector-zoned rims, and type-II aegirine begins replacing amphibole along with Fe- and Ti-oxides.

745 The drop in REE concentration in hydrothermal aegirine of all complexes shows that REE hydrothermal

746 enrichment is globally less effective than magmatic REE enrichment, but still effective. The observed REE

747 fractionation in all complexes show that hydrothermal fluids also have the ability to fractionate LREE-HREE

748 through their transportation associated with ligands such as $F^-$, $Cl^-$. The rate of fractionation as well as the

749 amount of mobilized REE depends on the local properties of the circulating fluid(s). These observations show

750 that hydrothermal flow is mandatory in order to enhance the concentration of the REE, and specially HREE, in

751 alkaline pegmatites to ore levels.

752

753 **References**

754 Ancey M, Bastenaire F, Tixier R (1978) Application des méthodes statistiques en microanalyse. Microanal
755       Microsc Électronique À Balayage 323:11–16

756 Arzamastsev AA, Arzamastseva LV, Zaraiskii GP (2011) Contact interaction of agpaitic magmas with basement
757       gneisses: an example of the Khibina and Lovozero massifs. Petrology 19:109–133

758 Barkov AY, Martin RF (2015) Anomalous Cr-rich zones in sector-zoned clinopyroxene macrocrysts in gabbro,
759       Mont Royal, Montreal, Quebec, Canada. Can Mineral 53:895–910

760 Beard C, van Hinsberg V, Stix J, Wilke M (2020) The effect of fluorine on clinopyroxene / melt trace-element
761       partitioning. Contrib Mineral Petrol. https://doi.org/doi: 10.1007/s00410-020-1672-5

762 Beard CD, van Hinsberg VJ, Stix J, Wilke M (2019) Clinopyroxene/melt trace element partitioning in sodic
763       alkaline magmas. J Petrol. https://doi.org/10.1093/petrology/egz052

764 Boily M, Williams-Jones AE (1994) The role of magmatic and hydrothermal processes in the chemical evolution
765       of the Strange Lake plutonic complex, Quebec-Labrador. Contrib Mineral Petrol 118:33–47

766 Bonin B (1988) Peralkaline granites in Corsica: some petrological and geochemical constraints. Rendiconti Della
767       Soc Ital Mineral E Petrol 73:1191–1194

768 Bonin B (2007) A-type granites and related rocks: evolution of a concept, problems and prospects. Lithos 97:1–
769       29

770 Bonin B (1990) Les granites des complexes annulaires, BRGM. Office des publications universitaires

771 Bonin B, Grelou-Orsini C, Vialette Y (1978) Age, origin and evolution of the anorogenic complex of Evisa
772       (Corsica): A K-Li-Rb-Sr study. Contrib Mineral Petrol 65:425–432

773    Bonin B, Platevoet B, Poitrasson F, Renna MR (2008) Eurogranites-IGCP510 2008 Joint Field-meeting—
774          Alkaline The Permian–Triassic A-type Volcanic–Plutonic Igneous Suite of Corsica. In: 33th
775          International Geological Congress in Oslo, Norway Convention Centre, Lillestrom, Norway

776    Borst AM, Friis H, Andersen T, et al (2016) Zirconosilicates in the kakortokites of the Ilímaussaq complex,
777          South Greenland: Implications for fluid evolution and high-field-strength and rare-earth element
778          mineralization in agpaitic systems. Mineral Mag 80:5–30

779    Bottazzi P, Tiepolo M, Vannucci R, et al (1999) Distinct site preferences for heavy and light REE in amphibole
780          and the prediction of Amph/L D REE. Contrib Mineral Petrol 137:36–45

781    Brousse R, Rançon JP (1984) Crystallization trends of pyroxenes from agpaitic phonolites (Cantal, France).
782          Mineral Mag 48:39–45

783    Chakhmouradian AR, Wall F (2012) Rare earth elements: minerals, mines, magnets (and more). Elements
784          8:333–340

785    Chakhmouradian AR, Zaitsev AN (2012) Rare earth mineralization in igneous rocks: sources and processes.
786          Elements 8:347–353

787    Chengyu W, Dianhao H, Zhongxun G (1990) REE Geochemistry in the Weathered Crust of Granites, Longnan
788          Area, Jiangxi Province. Acta Geol Sin - Engl Ed 3:193–209. https://doi.org/10.1111/j.1755-
789          6724.1990.mp3002006.x

790    Cocherie A, Rossi P, Fanning CM, Guerrot C (2005) Comparative use of TIMS and SHRIMP for U–Pb zircon
791          dating of A-type granites and mafic tholeiitic layered complexes and dykes from the Corsican Batholith
792          (France). Lithos 82:185–219

793    Coint N, Barnes CG, Yoshinobu AS, et al (2013) Use of trace element abundances in augite and hornblende to
794          determine the size, connectivity, timing, and evolution of magma batches in a tilted batholith.
795          Geosphere 9:1747–1765

796    Cucciniello C, Tucker RD, Jourdan F, et al (2016) The age and petrogenesis of alkaline magmatism in the
797          Ampasindava Peninsula and Nosy Be archipelago, northern Madagascar | SpringerLink. Mineral Petrol
798          110:309–331. https://doi.org/10.1007/s00710-015-0387-1

799    Currie KL (1985) An unusual peralkaline granite near lac Brisson, Quebec-Labrador. Curr Res 73–80

800    Deer WA, Howie RA, Zussman J (1997a) Rock-Forming Minerals: Single-chain Silicates, Volume 2A.
801          Geological Society of London

802    Deer WA, Howie RA, Zussman J (1997b) Rock-forming Minerals: Double-Chain Silicates, Volume 2B.
803          Geological Society of London

804    Diehl M (1990) Geology, mineralogy, geochemistry and hydrothermal alteration of the Brandberg alkaline
805          complex, Namibia. Geological Survey of Namibia

806    Donnot M (1963) Côte Nord-Ouest du complexe intrusif alcalin; Ampasindava-Manongarivo

807    Droop GTR (1987) A general equation for estimating Fe 3+ concentrations in ferromagnesian silicates and
808          oxides from microprobe analyses, using stoichiometric criteria. Mineral Mag 51:431–435

809    Duggan MB (1988) Zirconium-rich sodic pyroxenes in felsic volcanics from the Warrumbungle Volcano,
810          Central New South Wales, Australia. Mineral Mag 52:491–496

811    Dyulgerov MM, Platevoet B (2006) Unusual Ti and Zr aegirine-augite and potassic magnesio-arfvedsonite in the
812          peralkaline potassic oversaturated Buhovo-Seslavtzi complex, Bulgaria. Eur J Mineral 18:127–138

813    Estrade G (2014) Le complexe cénozoïque alcalin d'Ambohimirahavavy à Madagascar : origine, évolution et
814          minéralisations en métaux rares. Toulouse 3

815 Estrade G, Béziat D, Salvi S, et al (2014a) Unusual evolution of silica-under-and-oversaturated alkaline rocks in
816     the Cenozoic Ambohimirahavavy Complex (Madagascar): Mineralogical and geochemical evidence.
817     Lithos 206:361–383

818 Estrade G, Salvi S, Béziat D, et al (2014b) REE and HFSE mineralization in peralkaline granites of the
819     Ambohimirahavavy alkaline complex, Ampasindava peninsula, Madagascar. J Afr Earth Sci 94:141–
820     155

821 Estrade G, Salvi S, Béziat D (2018) Crystallization and destabilization of eudialyte-group minerals in peralkaline
822     granite and pegmatite: a case study from the Ambohimirahavavy complex, Madagascar. Mineral Mag
823     82:375–399. https://doi.org/10.1180/minmag.2017.081.053

824 European Commission (2018) Report on Critical Raw Materials and the Circular Economy.
825     http://ec.europa.eu/docsroom/documents/27348. Accessed 25 Apr 2018

826 Fedele L, Lustrino M, Melluso L, et al (2015) Trace-element partitioning between plagioclase, alkali feldspar,
827     Ti-magnetite, biotite, apatite, and evolved potassic liquids from Campi Flegrei (Southern Italy). Am
828     Mineral 100:233–249

829 Ferguson AK (1973) On hour-glass sector zoning in clinopyroxene. Mineral Mag 39:321–325.
830     https://doi.org/10.1180/minmag.1973.039.303.08

831 Flower MF (1974) Phase relations of titan-acmite in the system Na2O-Fe2O3-Al2O3-TiO2-SiO2 at 1000 bars
832     total water pressure. Am Mineral J Earth Planet Mater 59:536–548

833 Foland KA, Landoll JD, Henderson CMB, Chen J (1993) Formation of cogenetic quartz and nepheline syenites.
834     Geochim Cosmochim Acta 57:697–704. https://doi.org/10.1016/0016-7037(93)90380-F

835 Goodenough KM, Wall F, Merriman D (2018) The Rare Earth Elements: Demand, Global Resources, and
836     Challenges for Resourcing Future Generations. Nat Resour Res 27:201–216.
837     https://doi.org/10.1007/s11053-017-9336-5

838 Gowans RM, Lewis WJ, Zalnieriunas RV (2017) Quest Rare Minerals Ltd.: Strange Lake Resource Estimation

839 Grigor'eva AA, Zubkova NV, Pekov IV, et al (2011) Crystal chemistry of elpidite from Khan Bogdo (Mongolia)
840     and its K-and Rb-exchanged forms. Crystallogr Rep 56:832

841 Gysi AP, Williams-Jones AE, Collins P (2016) Lithogeochemical vectors for hydrothermal processes in the
842     Strange Lake peralkaline granitic REE-Zr-Nb deposit. Econ Geol 111:1241–1276

843 Hatch GP (2015) TMR Advanced Rare-Earth Projects Index — Technology Metals Research.
844     http://www.techmetalsresearch.com/metrics-indices/tmr-advanced-rare-earth-projects-index/. Accessed
845     27 Jun 2018

846 Hawthorne FC, Oberti R, Cannillo E, et al (2001) Li-bearing arfvedsonitic amphiboles from the Strange Lake
847     peralkaline granite, Quebec. Can Mineral 39:1161–1170

848 Hawthorne FC, Oberti R, Harlow GE, et al (2012) Nomenclature of the amphibole supergroup. Am Mineral
849     97:2031–2048

850 Hawthorne FC, Oberti R, Ungaretti L, et al (1996) Fluor-ferro-leakeite, NaNa2 (Fe2+ 2Fe3+ 2Li) Si8O22F2, a
851     new alkali amphibole from the Canada Pinabete pluton, Questa, New Mexico, USA. Am Mineral
852     81:226–228

853 Ishihara S, Hua R, Hoshino M, Murakami H (2008) REE abundance and REE minerals in granitic rocks in the
854     Nanling range, Jiangxi Province, southern China, and generation of the REE-rich weathered crust
855     deposits. Resour Geol 58:355–372

856 Jones AP, Peckett A (1981) Zirconium-bearing aegirines from Motzfeldt, south Greenland. Contrib Mineral
857     Petrol 75:251–255

858  Keppler H, Wyllie PJ (1991) Partitioning of Cu, Sn, Mo, W, U, and Th between melt and aqueous fluid in the
859      systems haplogranite-H 2 O- HCl and haplogranite-H 2 O- HF. Contrib Mineral Petrol 109:139–150

860  Kogarko LN, Williams CT, Woolley AR (2002) Chemical evolution and petrogenetic implications of loparite in
861      the layered, agpaitic Lovozero complex, Kola Peninsula, Russia. Mineral Petrol 74:1–24

862  Kovalenko VI, Yarmoluyk VV, Sal'nikova EB, et al (2006) Geology, geochronology, and geodynamics of the
863      Khan Bogd alkali granite pluton in southern Mongolia. Geotectonics 40:450–466

864  Kovalenko VI, Yarmolyuk VV (1995) Endogenous rare metal ore formations and rare metal metallogeny of
865      Mongolia. Econ Geol 90:520–529

866  Kramm U, Kogarko LN (1994) Nd and Sr isotope signatures of the Khibina and Lovozero agpaitic centres, Kola
867      Alkaline province, Russia. Lithos 32:225–242. https://doi.org/10.1016/0024-4937(94)90041-8

868  Kynicky J, Chakhmouradian AR, Xu C, et al (2011) Distribution and evolution of zirconium mineralization in
869      peralkaline granites and associated pegmatites of the Khan Bogd complex, southern Mongolia. Can
870      Mineral 49:947–965

871  Lacroix A (1923) Minéralogie de Madagascar. A. Challamel, éditeur, Librairie maritime et coloniale

872  Lagarec K, Rancourt DG (1997) Extended Voigt-based analytic lineshape method for determining N-
873      dimensional correlated hyperfine parameter distributions in Mössbauer spectroscopy. Nucl Instrum
874      Methods Phys Res Sect B Beam Interact Mater At 129:266–280

875  Larsen LM (1976) Clinopyroxenes and coexisting mafic minerals from the alkaline Ilimaussaq intrusion, South
876      Greenland. J Petrol 17:258–290

877  Larsen LM (1981) Sector zoned aegirine from the Ilímaussaq alkaline intrusion, South Greenland. Contrib
878      Mineral Petrol 76:285–291

879  Larsen LM, Sørensen H (1987) The Ilímaussaq intrusion—progressive crystallization and formation of layering
880      in an agpaitic magma. Geol Soc Lond Spec Publ 30:473–488

881  Leake BE, Woolley AR, Arps CE, et al (1997) Nomenclature of amphiboles; report of the Subcommittee on
882      Amphiboles of the International Mineralogical Association Commission on new minerals and mineral
883      names. Mineral Mag 61:295–310

884  Li X-H, Li W-X, Li Q-L, et al (2010) Petrogenesis and tectonic significance of the 850 Ma Gangbian alkaline
885      complex in South China: evidence from in situ zircon U–Pb dating, Hf–O isotopes and whole-rock
886      geochemistry. Lithos 114:1–15

887  Liu Y, Chen Z, Yang Z, et al (2015) Mineralogical and geochemical studies of brecciated ores in the Dalucao
888      REE deposit, Sichuan Province, southwestern China. Ore Geol Rev 70:613–636.
889      https://doi.org/10.1016/j.oregeorev.2015.03.006

890  Locock AJ (2014) An Excel spreadsheet to classify chemical analyses of amphiboles following the IMA 2012
891      recommendations. Comput Geosci 62:1–11

892  London D (2008) Pegmatites. Sp. Pub. 10. Can Miner 347:

893  Lucas J, Lucas P, Le Mercier T, et al (2014) Rare earths: science, technology, production and use. Elsevier

894  Mahood GA, Stimac JA (1990) Trace-element partitioning in pantellerites and trachytes. Geochim Cosmochim
895      Acta 54:2257–2276. https://doi.org/10.1016/0016-7037(90)90050-U

896  Mann U, Marks M, Markl G (2006) Influence of oxygen fugacity on mineral compositions in peralkaline melts:
897      The     Katzenbuckel     volcano,     Southwest     Germany.     Lithos     91:262–285.
898      https://doi.org/10.1016/j.lithos.2005.09.004

899 Marks M, Halama R, Wenzel T, Markl G (2004) Trace element variations in clinopyroxene and amphibole from
900         alkaline to peralkaline syenites and granites: implications for mineral–melt trace-element partitioning.
901         Chem Geol 211:185–215

902 Marks MA, Markl G (2017) A global review on agpaitic rocks. Earth-Sci Rev 173:229–258

903 Migdisov A, Williams-Jones AE, Brugger J, Caporuscio FA (2016) Hydrothermal transport, deposition, and
904         fractionation of the REE: Experimental data and thermodynamic calculations. Chem Geol 439:13–42

905 Miller RM (1983) The Pan-African Damara Orogen of South West Africa/Namibia. Evol Damara Orogen South
906         West Afr

907 Miller RR (1996) Structural and textural evolution of the Strange Lake peralkaline rare-element (NYF) granitic
908         pegmatite, Quebec-Labrador. Can Mineral 34:349–371

909 Mollo S, Blundy JD, Giacomoni P, et al (2017) Clinopyroxene-melt element partitioning during interaction
910         between trachybasaltic magma and siliceous crust: Clues from quartzite enclaves at Mt. Etna volcano.
911         Lithos 284–285:447–461. https://doi.org/10.1016/j.lithos.2017.05.003

912 Moore M, Chakhmouradian AR, Mariano AN, Sidhu R (2015) Evolution of rare-earth mineralization in the Bear
913         Lodge carbonatite, Wyoming: Mineralogical and isotopic evidence. Ore Geol Rev 64:499–521.
914         https://doi.org/10.1016/j.oregeorev.2014.03.015

915 Morimoto N (1988) Nomenclature of Pyroxenes. Mineral Petrol 39:55–76

916 Nakamura Y (1973) Origin of sector-zoning of igneous clinopyroxenes. Am Mineral 58:986–990

917 Nardi LVS, Bitencourt M de F (2009) A-type granitic rocks in post-collisional settings in southernmost Brazil:
918         their classification and relationship with tectonics and magmatic series. Can Mineral 47:1493–1503.
919         https://doi.org/10.3749/canmin.47.6.1493

920 Nielsen TFD (1979) The occurrence and formation of Ti-aegirines in peralkaline syenites. Contrib Mineral
921         Petrol 69:235–244

922 Ortoleva P, Merino E, Moore C, Chadam J (1987) Geochemical self-organization I; reaction-transport feedbacks
923         and modeling approach. Am J Sci 287:979–1007

924 Pennycook SJ, Nellist PD (2011) Scanning Transmission Electron Microscopy: Imaging and Analysis. Springer
925         Science & Business Media

926 Piilonen PC, McDonald AM, Lalonde AE (1998) The crystal chemistry of aegirine from Mont Saint-Hilaire,
927         Quebec. Can Mineral 36:779–791

928 Pillet D, Bonhomme MG, Duthou JL, Chenevoy M (1989) Chronologie Rb/Sr et K/Ar du granite peralcalin du
929         lac Brisson, Labrador central, Nouveau-Québec. Can J Earth Sci 26:328–332

930 Poitrasson F, Duthou J-L, Pin C (1995) The relationship between petrology and Nd isotopes as evidence for
931         contrasting anorogenic granite genesis: example of the Corsican Province (SE France). J Petrol
932         36:1251–1274

933 Poitrasson F, Paquette J-L, Montel J-M, et al (1998) Importance of late-magmatic and hydrothermal fluids on the
934         Sm–Nd isotope mineral systematics of hypersolvus granites. Chem Geol 146:187–203

935 Rakotovao S, Rakotondrazafy R, Beziat D, et al (2009) Pétrologie du complexe alcalin cénozoïque
936         d'Ambohimirahavavy, presqu'île d'Ampasindava, nord-ouest de Madagascar. Mada-Géo 13:2–19

937 Ranløv J, Dymek RF (1991) Compositional zoning in hydrothermal aegirine from fenites in the Proterozoic
938         Gardar Province, South Greenland. Eur J Mineral 837–854. https://doi.org/10.1127/ejm/3/5/0837

939 Roelofsen JN (1997) The primary and secondary mafic silicates of two alkaline anorogenic complexes: Strange
940     Lake (Quebec-Labrador) and Amba Dongar (Gujarat, India). PhD Thesis, McGill University Libraries

941 Rønsbo JG, Pedersen AK, Engell J (1977) Titan-aegirine from early Tertiary ash layers in northern Denmark.
942     Lithos 10:193–204

943 Salvi S, William-Jones A (1995) Zirconosilicate phase relations in the Strange Lake (Lac Brisson) pluton,
944     Quebec-Labrador, Canada: American Mineralogist. Am Mineral 80:1031–1040.
945     https://doi.org/10.2138/am-1995-9-1019

946 Salvi S, Williams-Jones AE (1990) The role of hydrothermal processes in the granite-hosted Zr, Y, REE deposit
947     at Strange Lake, Quebec/Labrador: evidence from fluid inclusions. Geochim Cosmochim Acta
948     54:2403–2418

949 Salvi S, Williams-Jones AE (2006) Alteration, HFSE mineralisation and hydrocarbon formation in peralkaline
950     igneous systems: Insights from the Strange Lake Pluton, Canada. Lithos 91:19–34

951 Salvi S, Williams-Jones AE (1996) The role of hydrothermal processes in concentrating high-field strength
952     elements in the Strange Lake peralkaline complex, northeastern Canada. Geochim Cosmochim Acta
953     60:1917–1932

954 Salvi S, Williams-Jones AE (1997) Fischer-Tropsch synthesis of hydrocarbons during sub-solidus alteration of
955     the Strange Lake peralkaline granite, Quebec/Labrador, Canada. Geochim Cosmochim Acta 61:83–99

956 Sanematsu K, Kon Y, Imai A, et al (2013) Geochemical and mineralogical characteristics of ion-adsorption type
957     REE mineralization in Phuket, Thailand. Miner Deposita 48:437–451. https://doi.org/10.1007/s00126-
958     011-0380-5

959 Schmitt AK, Trumbull RB, Dulski P, Emmermann R (2002) Zr-Nb-REE mineralization in peralkaline granites
960     from the Amis Complex, Brandberg (Namibia): evidence for magmatic pre-enrichment from melt
961     inclusions. Econ Geol 97:399–413

962 Shannon RD (1976) Revised effective ionic radii and systematic studies of interatomic distances in halides and
963     chalcogenides. Acta Crystallogr 32:751–767

964 Sheard ER, Williams-Jones AE, Heiligmann M, et al (2012) Controls on the Concentration of Zirconium,
965     Niobium, and the Rare Earth Elements in the Thor Lake Rare Metal Deposit, Northwest Territories,
966     Canada. Econ Geol 107:81–104. https://doi.org/10.2113/econgeo.107.1.81

967 Shearer CK, Larsen LM (1994) Sector-zoned aegirine from the Ilimaussaq alkaline intrusion, South Greenland:
968     Implications for trace-element behavior in pyroxene. Am Mineral 79:340–352

969 Siegel K, Williams-Jones AE, Stevenson R (2017a) A Nd-and O-isotope study of the REE-rich peralkaline
970     Strange Lake granite: implications for Mesoproterozoic A-type magmatism in the Core Zone (NE-
971     Canada). Contrib Mineral Petrol 172:54

972 Siegel K, Williams-Jones AE, van Hinsberg VJ (2017b) The amphiboles of the REE-rich A-type peralkaline
973     Strange Lake pluton–fingerprints of magma evolution. Lithos 288:156–174

974 Smith MP (2007) Metasomatic silicate chemistry at the Bayan Obo Fe–REE–Nb deposit, Inner Mongolia, China:
975     contrasting chemistry and evolution of fenitising and mineralising fluids. Lithos 93:126–148

976 Smith MP, Henderson P, Jeffries TER, et al (2004) The rare earth elements and uranium in garnets from the
977     Beinn an Dubhaich Aureole, Skye, Scotland, UK: constraints on processes in a dynamic hydrothermal
978     system. J Petrol 45:457–484

979 Strong DF (1969) Formation of the hour-glass structure in augite. Mineral Mag 37:472–479

980 Sun S-S, McDonough W (1989) Chemical and isotopic systematics of oceanic basalts: implications for mantle
981     composition and processes. Geol Soc Lond Spec Publ 42:313–345

982    Thomas RJ, De Waele B, Schofield DI, et al (2009) Geological evolution of the Neoproterozoic Bemarivo Belt,
983        northern Madagascar. Precambrian Res 172:279–300. https://doi.org/10.1016/j.precamres.2009.04.008

984    Trail D, Bruce Watson E, Tailby ND (2012) Ce and Eu anomalies in zircon as proxies for the oxidation state of
985        magmas. Geochim Cosmochim Acta 97:70–87. https://doi.org/10.1016/j.gca.2012.08.032

986    U. S. Geological Survey (2019) Rare Earths Statistics and Information. In: Miner. Commod. Summ.
987        https://www.usgs.gov/centers/nmic/rare-earths-statistics-and-information. Accessed 28 Aug 2019

988    Ubide T, McKenna CA, Chew DM, Kamber BS (2015) High-resolution LA-ICP-MS trace element mapping of
989        igneous     minerals:     In     search     of     magma     histories.     Chem     Geol     409:157–168.
990        https://doi.org/10.1016/j.chemgeo.2015.05.020

991    Ubide T, Mollo S, Zhao J, et al (2019) Sector-zoned clinopyroxene as a recorder of magma history, eruption
992        triggers,     and     ascent     rates.     Geochim     Cosmochim     Acta     251:265–283.
993        https://doi.org/10.1016/j.gca.2019.02.021

994    Vasyukova O, Williams-Jones A (2020) Partial melting, fractional crystallisation, liquid immiscibility and
995        hydrothermal mobilisation–A `Recipe'for the formation of economic A-Type granite-hosted HFSE
996        deposits. Lithos 356:105300

997    Vasyukova O, Williams-Jones AE (2014) Fluoride–silicate melt immiscibility and its role in REE ore formation:
998        Evidence from the Strange Lake rare metal deposit, Québec-Labrador, Canada. Geochim Cosmochim
999        Acta 139:110–130

1000   Vasyukova OV, Williams-Jones AE (2019) Closed system fluid-mineral-mediated trace element behaviour in
1001       peralkaline rare metal pegmatites: Evidence from Strange Lake. Chem Geol 505:86–99

1002   Vasyukova OV, Williams-Jones AE, Blamey NJF (2016) Fluid evolution in the Strange Lake granitic pluton,
1003       Canada: Implications for HFSE mobilisation. Chem Geol 444:83–100

1004   Veksler IV, Dorfman AM, Dulski P, et al (2012) Partitioning of elements between silicate melt and immiscible
1005       fluoride, chloride, carbonate, phosphate and sulfate melts, with implications to the origin of
1006       natrocarbonatite. Geochim Cosmochim Acta 79:20–40. https://doi.org/10.1016/j.gca.2011.11.035

1007   Wang Q, Deng J, Liu X, et al (2010) Discovery of the REE minerals and its geological significance in the
1008       Quyang     bauxite     deposit,     West     Guangxi,     China.     J     Asian     Earth     Sci     39:701–712.
1009       https://doi.org/10.1016/j.jseaes.2010.05.005

1010   William-Jones AE, Migdisov AA, Samson IM (2012) Hydrothermal mobilisation of the Rare Earth Elements–a
1011       Tale of" Ceria" and" Yttria. Elements 8:355–360

1012   Xu C, Kynickỳ J, Smith MP, et al (2017) Origin of heavy rare earth mineralization in South China. Nat Commun
1013       8:14598

1014   Yang X-M, Yang X-Y, Zheng Y-F, Le Bas MJ (2003) A rare earth element-rich carbonatite dyke at Bayan Obo,
1015       Inner Mongolia, North China. Mineral Petrol 78:93–110

1016   Zaitsev AN, Terry Williams C, Jeffries TE, et al (2014) Rare earth elements in phoscorites and carbonatites of
1017       the Devonian Kola Alkaline Province, Russia: Examples from Kovdor, Khibina, Vuoriyarvi and Turiy
1018       Mys complexes. Ore Geol Rev 61:204–225. https://doi.org/10.1016/j.oregeorev.2014.02.002

1019

1020

1021   **Tables caption**

1022

1023 **Table 1** Mean values for the major and trace element composition, obtained by microprobe and LA-ICPMS

1024 respectively, of amphiboles from pegmatites and granites from the six complexes. Abbreviations: no.: number of

1025 replicates; F-arf: fluoro-arfvedsonite; F-f-f-lea: ferro-ferri-fluoro-leakeite; F-f-kato: ferro-ferri-katophorite; b.d.l:

1026 below detection limit; Ambo: Ambohimirahavavy; KB: Khan bogd; M: Manongarivo; SL: Strange Lake

1027

1028 **Table 2** Mean values (number of analysis given in bold) for the major and trace element composition, obtained

1029 by microprobe and LA-ICPMS respectively, of aegirine from pegmatites and granites from six complexes

1030 worldwide in both pegmatites and granites. Granites only comprise type-II aegirine. T I, T II: aegirine type-I, II.

1031 Abbreviations: no.: number of replicates; b.d.l: below detection limit; Ambo: Ambohimirahavavy; KB: Khan

1032 bogd; M: Manongarivo; SL: Strange Lake

1033

1034 **Table 3** Mean composition of cores and rims of type-I aegirine from 5 complexes. Abbreviations: no.: number of

1035 replicates; b.d.l: below detection limit; Ambo: Ambohimirahavavy; KB: Khan bogd; M: Manongarivo

1036

1037 **Figures caption**

1038

1039 **Fig. 1** A logarithmic diagram plotting chondrite-normalized (Sun and McDonough 1989) values of whole-rock

1040 Yb/La vs Yb contents for different alkaline complexes worldwide. Five groups are distinguished: alkaline

1041 granites, alkaline pegmatites, carbonatites, nepheline syenites, and ion-adsorption deposits. Data are from this

1042 study plus from Estrade et al. (2014b), Boily and Williams-Jones (1994), Estrade (2014), Kynicki et al. (2011),

1043 Poitrasson et al. (1995), Vasyukova and Williams-Jones (2014), Schmitt et al. (2002), Moore et al. (2015), Yang

1044 et al. (2003), Xu et al. (2017), Liu et al. (2015), Zaitsev et al. (2014), Kogarko et al. (2002), Li et al. (2010),

1045 Sørensen et al. (1987), Hatch (2015), Sanematsu et al. (2013), Ishihara et al. (2008), Wang et al. (2010), and

1046 Chengyu et al. (1990)

1047

1048  **Fig. 2** Map localizing the six complexes studied in this paper. The geodynamic context and ages are given

1049 below their names in the rectangular boxes

1050

1051 **Fig. 3** Photographs of outcrop or hand samples of pegmatites from the six complexes. Most display a well-

1052 marked layering defined by mineralogy and textural variations

1053

1054 **Fig. 4 a** Altered astrophyllite from Amis, **b** REE-bearing pseudomorph (Manongarivo), **c** Zircon-quartz

1055 pseudomorph (Evisa), **d** Elpidite (Khan Bogd), altered to armstrongite and zircon in its center, **e** Arfvedsonite

1056 replaced by type-II aegirine (Evisa), **f** A type-I aegirine showing core to rim zoning (Ambohimirahavavy), **g**

1057 Two tiny fluid inclusions in the rim of a type-I crystal of aegirine (Khan Bogd), **h** Mineral inclusions contained

1058 within the rim of a type-I aegirine (Ambohimirahavavy) that are of the same nature than minerals in REE-

1059 bearing pseudomorph, **i** A single crystal of type-II aegirine (Strange Lake), **j** Zoned amphibole, from katophorite

1060 in the core to arfvedsonite in the rims (Evisa), **k** A type-I aegirine showing core to rim zoning with zone B (Khan

1061 Bogd), **l** Zoned amphibole, from arfvedsonite in the core to leakeite in the rims (Evisa). Photographs **a, c, e, f, g,**

1062 **i** and **k** were taken with an optical microscope; photographs **b, h, j** and **l** with SEM EDS; and **d** with optical

1063 cathodoluminescence. pseudom: pseudomorph; zrn: zircon; aeg: aegirine; amph: amphiboles; qtz: quartz; afs:

1064 alkali feldspar; bsn: bastnäsite-(Ce); arf: arfvedsonite; ox: Ti- and Fe-oxides; calh: calciohilairite; CKZ:

1065 unidentified Ca- and K-bearing zirconosilicates; CMZ: unidentified Ca- and Mn-bearing zirconosilicates;

1066 NbYsil: unidentified Nb- and Y-bearing silicate; arm: armstrongite; elp: elpidite; astr: astrophyllite

1067

1068 **Fig. 5** Chemical composition of amphiboles. **a, b, c** Ternary diagrams representing amphibole poles for the **a**

1069 Evisa and Manongarivo complexes; **b** Ambohimirahavavy and Amis complexes; **c** Khan Bogd and Strange Lake

1070 complexes. Poles are plotted as 10 Mg and 10 Ca for a better visualization of the dataset. **d** Boxplots showing the

1071 trace-element composition of amphiboles from the different complexes. Thick black line represents the median,

1072 upper and lower boxplot limits the first and third quartile respectively, upper and lower dashed lines are the

1073 maximum and minimum values respectively, and the thin black line is the detection limit. Areas are shaded to

1074 distinguish data for each complex M: Manongarivo; Amb: Ambohimirahavavy; SL: Strange Lake; KB: Khan

1075 Bogd

1076

1077 **Fig. 6** Microprobe and LA-ICPMS maps on a type-I aegirine crystal at Ambohimirahavavy. Visible zonations

1078 were also found in the other complexes (see Supplementary material). 3 zones are distinguished: the core A, and

1079 the sector-zoned rims Cand D. Microprobe maps are in wt%, and LA-ICPMS maps are in ppm. Limits of

1080    aegirine on LA-ICPMS maps are blurry because the signal from the crystal and the matrix mix and do not reflect

1081    an actual concentration

1082

1083    **Fig. 7** Chemical composition of type-I and type-II aegirine crystals. Type-I aegirine is split between core and

1084    rim. Core and rim analyses are identified for Type-I aegirine. **a, b, c** are for aegirine, (Ti, Zr)-aegirine, and

1085    clinoferrosilite; when figures; **d, e, f** are for aegirine + (Ti, Zr)-aegirine, hedenbergite, and clinoferrosilite. **a, d**

1086    complexes Evisa and Manongarivo; **b, e** complexes Ambohimirahavavy and Amis; **c, f** Khan Bogd and Strange

1087    Lake; **g** Box diagrams comparing the trace element contents of aegirine from the different complexes. Thick

1088    black line represents the median, upper and lower boxplot limits the first and third quartile respectively, upper

1089    and lower dashed lines are the maximum and minimum values respectively, and the thin black line is the

1090    detection limit. Colours are keyed to the legend given in **a-f**. Areas are shaded to distinguish data for each

1091    complex

1092

1093    **Fig. 8** Logarithmic diagrams plotting chondrite-normalized REE composition obtained by LA-ICP-MS for

1094    amphiboles (normalization from Sun and McDonough, 1989) for all six complexes

1095

1096    **Fig. 9** Logarithmic diagrams plotting chondrite-normalized REE composition obtained by LA-ICPMS for

1097    aegirine (normalization from Sun and McDonough, 1989) for all six complexes. Large spectra presents all LA-

1098    ICP-MS analyses for type-I and type-II aegirine, whereas small spectra on the side show an example of analyses

1099    performed on a single type-I crystal

1100

1101    **Fig. 10** Diagram plotting REE concentration obtained by LA-ICPMS in the core and rim of type-I pyroxene in 5

1102    complexes. The typical analytical error is provided by the cross on the top right corner and is similar for all

1103    provided analyses

1104

1105    **Fig. 11** Histograms plotting the difference of REE concentration between the core and the rims of type-I

1106    aegirine, and thereby REE fractionation from core to rim. Negative values stand for a higher REE concentration

36

1107 in the core, and positive ones for a higher concentration in the rims. The rim enrichment in Khan Bogd is an

1108 artifact. Calculated error is shown by black lines at the end of the histogram bars

1109

1110 **Fig. 12** A schematic illustration of a model for aegirine and amphiboles formation. The arrows signify transfer of

1111 elements (in the boxes) to the different minerals from the melt or fluid (light blue), the line thickness is

1112 proportional to the amount of transfer, and a dashed line indicates a possible transfer. Ligands in the fluids are

1113 also shown. During the early magmatic stage, the competition for REE, Zr, Hf, Zr and Sn is low to moderate

1114 (depending on the co-presence or not of amphibole, pyroxene and complex zirconosilicate) and allows a relative

1115 enrichment in these elements in type-I aegirine and, mostly for REE, in amphibole. During the hydrothermal

1116 stage, the competition for these elements is stronger as it involves zircon and REE-bearing minerals;

1117 consequently, type-I aegirine rims are globally depleted. Fluids composition leads to a different mobilization of

1118 light and heavy REE, originating REE fractionation. Meanwhile, hydrothermal fluids replace amphiboles by

1119 type-II secondary aegirine and Fe-Ti-oxides

1120

1121 **Electronic Supplementary Material**

1122 **Online Resource 1** Text and maps detailing the geological background of all six studied complexes

1123

1124 **Online Resource 2** Table of standards used for calibration of EPMA and associated detection limits.

1125 Abbreviation: n.a.: not analyzed

1126

1127 **Online Resource 3** Table of detection limits for in situ LA-ICPMS measurements

1128

1129 **Online Resource 4** Microprobe maps on a type-I aegirine crystal at Amis. 3 zones are distinguished: A, the core

1130 rich in Ca, Zr, Sn, Hf and poor in Na, Fe; C, sector zoning rich in Ti, Ca; and D, sector zoning rich in Fe. The

1131 thick line represents limits of the map

1132

1133     **Online Resource 5** Microprobe maps on a type-I aegirine crystal at Evisa. 3 zones are distinguished: A, the

1134     core rich in Ca, Zr, Sn, Hf and poor in Na, Fe; C, sector zoning rich in Ti, Ca; and D, sector zoning rich in Fe.

1135     The thick line represents limits of the map

1136

1137     **Online Resource 6** Microprobe maps on a type-I aegirine crystal at Khan Bogd. 4 zones are distinguished: A,

1138     the core rich in Ca, Zr, Sn, Hf and poor in Na, Fe; B; C, sector zoning rich in Ti, Ca; and D, sector zoning rich in

1139     Fe

1140

1141     **Online Resource 7** Microprobe maps on a type-I aegirine crystal at Manongarivo. 3 zones are distinguished: A,

1142     the core rich in Ca, Zr, Sn, Hf and poor in Na, Fe; C, sector zoning rich in Ti, Ca; and D, sector zoning rich in Fe

1143

1144     **Online Resource 8** Microprobe maps on a type-II aegirine crystal at Strange Lake. No core-to-rim zoning is

1145     observed, but an oscillatory zoning occurs for most elements

1146